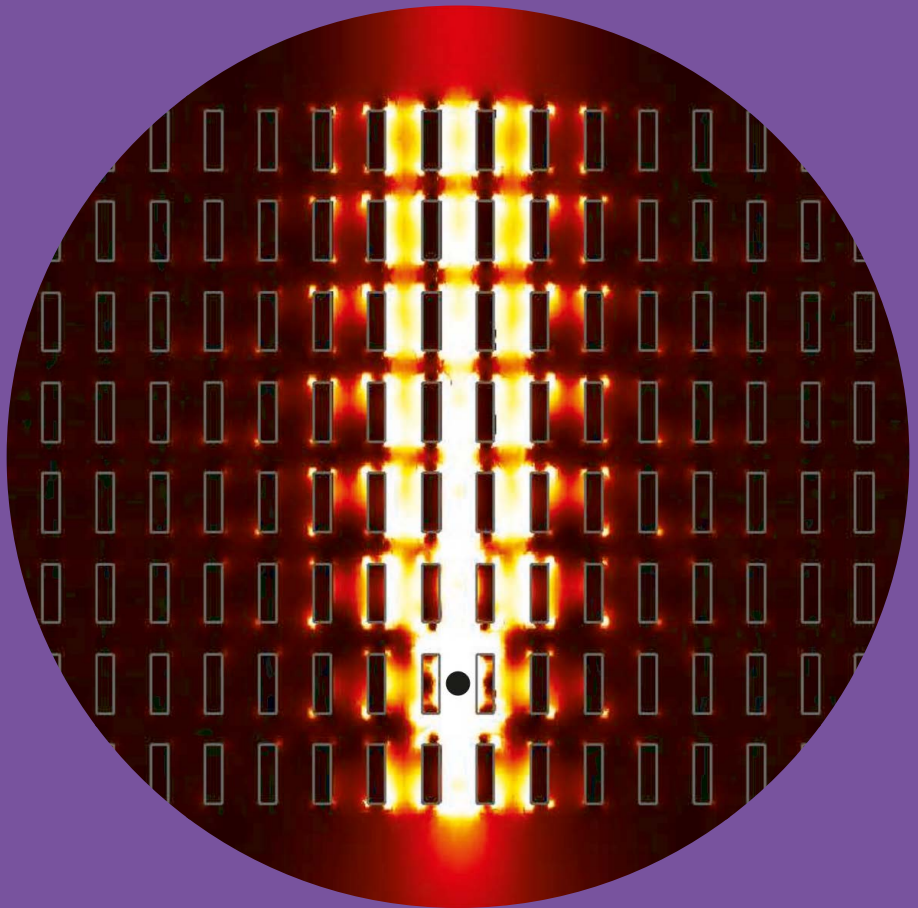


Nanophotonic control of optical emission, propagation, and all-optical modulation

Markus Nyman



Nanophotonic control of optical emission, propagation, and all-optical modulation

Markus Nyman

A doctoral dissertation completed for the degree of Doctor of Science (Technology) to be defended, with the permission of the Aalto University School of Science,
<https://aalto.zoom.us/j/69971363550>, on 25 March 2021 at 13.

**Aalto University
School of Science
Department of Applied Physics
Optics and Photonics**

Supervising professor

Prof. Matti Kaivola, Aalto University, Finland

Thesis advisor

Dr. Andriy Shevchenko, Aalto University, Finland

Preliminary examiners

Prof. Taco Visser, Vrije Universiteit Amsterdam, The Netherlands

Prof. Humeyra Caglayan, Tampere University, Finland

Opponent

Prof. Alexandre Dmitriev, University of Gothenburg, Sweden

Aalto University publication series

DOCTORAL DISSERTATIONS 28/2021

© 2021 Markus Nyman

ISBN 978-952-64-0288-8 (printed)

ISBN 978-952-64-0289-5 (pdf)

ISSN 1799-4934 (printed)

ISSN 1799-4942 (pdf)

<http://urn.fi/URN:ISBN:978-952-64-0289-5>

Unigrafia Oy

Helsinki 2021

Finland



Author

Markus Nyman

Name of the doctoral dissertation

Nanophotonic control of optical emission, propagation, and all-optical modulation

Publisher School of Science**Unit** Department of Applied Physics**Series** Aalto University publication series DOCTORAL DISSERTATIONS 28/2021**Field of research** Nano-optics, Photonics**Manuscript submitted** 9 December 2020**Date of the defence** 25 March 2021**Permission for public defence granted (date)** 18 February 2021**Language** English☐ **Monograph**☒ **Article dissertation**☐ **Essay dissertation****Abstract**

The field of nanophotonics is concerned with the use of nanoscale structures and systems to control light for purposes such as miniaturization of optical components and control over the emission of light by quantum emitters. The research compiled in this dissertation focuses on artificial optical nanomaterials, generation of light, and all-optical modulation.

Most of the artificial optical materials examined in this dissertation are metamaterials. These consist of scatterers, such as nanorods, in a lattice with a sub-wavelength period. For light passing through a metamaterial, the material appears as a homogeneous medium but with extraordinary optical properties. Typically, the optical properties also vary depending on the direction of light propagation; this effect is known as spatial dispersion. To analyze and design spatially dispersive metamaterials for different purposes, this dissertation adopts a wave parameter-based approach where a refractive index and wave impedance is assigned to each plane wave propagating in the metamaterial. We refine the previously-developed wave parameter theory to describe the movement of optical energy inside nanomaterials. We then develop a Fourier transform-based method to analyze optical emission inside spatially dispersive materials. We also discuss the outcoupling of light from inside nanomaterials, and show how emitted light can efficiently escape even from inside materials that exhibit strong attenuation. We then design and experimentally demonstrate nanostructures that drastically increase the brightness of a fluorescent film by combining the enhancements of radiation directivity and pump light absorption. The methods and ideas put forward in this part are useful for understanding and designing nanomaterials and structures for the purpose of controlling optical emission, with an eye on applications such as sensors and light sources.

The dissertation also discusses nanomaterials for controlling the polarization of light. We theoretically and experimentally demonstrate a wave plate that relies on the strong birefringence of a sub-wavelength metal-dielectric structure. The wave plate combines low loss, broad bandwidth, and operation in the transmission mode, and we also discuss how it can be fabricated on large areas, making mass production feasible.

Finally, we present a method of ultrafast all-optical modulation, as well as a method of ultrafast detection. Both methods rely on an optical gain medium and a Fourier transform pulse shaper. The on-resonance gain medium facilitates strong nonlinear interaction of two optical signals. The pulse shaper is used as a wavelength splitter and recombiner (in all-optical modulation) and a time-to-space mapper (in detection). In our experiments, modulation and detection reach sub-picosecond speed and resolution, respectively, despite the overall nanosecond-scale response of the gain medium.

Keywords optical nanomaterials, metamaterials, spontaneous emission, modulation**ISBN (printed)** 978-952-64-0288-8**ISBN (pdf)** 978-952-64-0289-5**ISSN (printed)** 1799-4934**ISSN (pdf)** 1799-4942**Location of publisher** Helsinki**Location of printing** Helsinki**Year** 2021**Pages** 149**urn** <http://urn.fi/URN:ISBN:978-952-64-0289-5>

Tekijä

Markus Nyman

Väitöskirjan nimi

Valon emission, etenemisen ja moduloinnin hallinta nanofotoniikan avulla

Julkaisija Perustieteiden korkeakoulu**Yksikkö** Teknillisen fysiikan laitos**Sarja** Aalto University publication series DOCTORAL DISSERTATIONS 28/2021**Tutkimusala** Nano-optiikka, fotonikka**Käsikirjoituksen pvm** 09.12.2020**Väitöspäivä** 25.03.2021**Väittelyluvan myöntämispäivä** 18.02.2021**Kieli** Englanti☐ **Monografia**☒ **Artikkeliväitöskirja**☐ **Esseeväitöskirja****Tiivistelmä**

Nanofotoniikka on valon manipulointia nanometrin kokoisilla rakenteilla. Nanofotoniikka mahdollistaa esimerkiksi hyvin pienten optisten komponenttien valmistamisen ja valon emission hallitsemisen mikroskooppisella tasolla. Tähän väitöskirjaan koottu tutkimus keskittyy keinoitekoisiin optisiin nanomateriaaleihin, valonlähteisiin ja optiseen modulointiin.

Väitöskirjassa tutkittavat keinoitekoiset optiset materiaalit ovat pääasiassa metamateriaaleja. Ne koostuvat sirottajista, esimerkiksi nanosauvoista, jotka ovat hilassa, jonka yksikkökopit ovat pienempiä kuin valon aallonpituus. Tällainen materiaali näyttäytyy valolle homogeenisena väliaineena, jolla voi olla erityislaatuista optisia ominaisuuksia. Useimmiten materiaalin optiset ominaisuudet myös riippuvat valon etenemissuunnasta: tätä kutsutaan spatiaaliseksi dispersioksi. Väitöskirjassa käytetään spatiaalisesti dispersiivisten materiaalien analyysiin ja suunnitteluun aaltoparametrimenetelmää, jossa jokaiselle materiaalissa etenevälle tasoaalolle määritetään oma taitekerroin ja aaltoimpedanssi. Täydennämme ensin aaltoparametriteoriaa, jotta sen avulla voidaan kuvata optisen energian etenemistä nanomateriaalien sisällä. Tämän jälkeen kehitämme Fourier-muunnokseen perustuvan menetelmän, jolla voidaan analysoida valon emissiota spatiaalisesti dispersiivisten nanomateriaalien sisällä. Tutkimme myös valon kytketymistä nanomateriaalien sisältä ulos, ja näytämme kuinka valo voi paeta tehokkaasti jopa valoa voimakkaasti vaimentavien materiaalien sisältä. Tämän jälkeen tutkimme teoreettisesti ja kokeellisesti nanorakenteita, jotka kasvattavat huomattavasti fluoresoivan kalvon kirkkautta yhdistäen parannuksia säteilyn suuntaavuuteen ja pumppausvalon absorptioon. Esitettyjä menetelmiä ja ideoita voidaan käyttää kehitettäessä nanorakenteita esimerkiksi antureita ja valonlähteitä varten.

Väitöskirja käsittelee myös nanomateriaaleja, jotka muuttavat valon polarisaatiota. Kehitämme aaltolevyn joka perustuu metalli-dielektrisen nanorakenteen vahvaan kahtaistaitavuuteen, ja tutkimme sen toimintaa teoreettisesti ja kokeellisesti. Tässä nanomateriaaliaaltolevyssä yhdistyvät pienet häviöt, laaja optinen kaistanleveys ja toiminta läpäisymoodissa. Näytämme myös, että nanorakenteesta huolimatta aaltolevy voidaan valmistaa alaltaan suureksi, mikä on massatuotannon edellytys.

Viimeisessä osuudessa esitämme ultranopean täysin optisen modulaatiomenetelmän sekä ultranopean valoilmaisimen. Molemmat perustuvat valoa vahvistavaan laserväliaineeseen ja Fourier-muuntavaan pulssinmuotoilijaan. Laserväliaine mahdollistaa kahden valosignaalin vahvan epälineaarisen vuorovaikutuksen. Pulssinmuotoilija puolestaan toimii aallonpituusjakajana ja -yhdistäjänä (modulaatiomenetelmässä) ja ajasta-paikkaan kuvauksen tekijänä (ilmaisimessa). Saavutamme kokeellisissa tuloksissamme alle pikosekunnin modulaationopeuden ja aikaresoluution huolimatta siitä, että laserväliaine toimii nanosekunnin aikaskaalassa.

Avainsanat optiset nanomateriaalit, metamateriaalit, spontaani emissio, modulointi**ISBN (painettu)** 978-952-64-0288-8**ISBN (pdf)** 978-952-64-0289-5**ISSN (painettu)** 1799-4934**ISSN (pdf)** 1799-4942**Julkaisupaikka** Helsinki**Painopaikka** Helsinki**Vuosi** 2021**Sivumäärä** 149**urn** <http://urn.fi/URN:ISBN:978-952-64-0289-5>

Preface

This dissertation is the result of my relentless pursuit of knowledge, a quest undertaken in collaboration with a number of people whom I would like to acknowledge.

To begin with, the scientific work compiled here was largely performed at the Optics and Photonics Group at the Department of Applied Physics of the Aalto University School of Science. I wish to thank my supervisor, Prof. Matti Kaivola, and my thesis advisor, Dr. Andriy Shevchenko, for all their advice, support and stimulating discussions. I also thank Prof. Alexander Dmitriev for acting as the opponent, and Prof. Taco Visser and Prof. Humeyra Caglayan for pre-examining the dissertation.

During this period, I have worked together with a number of people whose contributions and company have also been important. I wish to especially extend my gratitude to my long-time colleagues Dr. Ville Kivijärvi, Somendu Maurya, and Elena Ilina, as well as to Prof. Klas Lindfors and his research group for our collaboration in nanofabrication.

I also gratefully acknowledge the financial support provided by the Finnish Cultural Foundation for the research that led to this dissertation.

Espoo, February 23, 2021,

Markus Nyman

Contents

Preface	1
Contents	3
List of Publications	5
Author's Contribution	7
1. Introduction	11
1.1 Photonics and nanomaterials	11
1.2 All-optical modulation and detection	13
1.3 Structure of dissertation	15
2. Optical emission in nanomaterials	17
2.1 Metamaterials and spatial dispersion	17
2.2 Wave parameters	18
2.3 Optical emission	21
2.4 Electric-current decomposition method	23
2.5 Outcoupling of emission	25
2.6 Examples	27
2.6.1 Diffraction-compensating metamaterial	27
2.6.2 Metal-dielectric stack	29
3. Large-area fluorescence enhancement	33
3.1 Factors that influence fluorescence enhancement	34
3.2 Calculations	35
3.2.1 Directionality enhancement	35
3.2.2 Purcell factor	36
3.2.3 Pump enhancement	36
3.3 Experimental demonstration	37
4. Metamaterial polarization manipulation: a metal-dielectric wave plate	41

4.1	Nanostructures and birefringence	42
4.2	Design	43
4.3	Experimental demonstration	45
5.	Sub-picosecond all-optical modulation and detection	49
5.1	Optical nonlinearity at sub-picosecond time scales	49
5.2	Spectrally-addressed all-optical modulation	51
5.3	Ultrafast signal detection	53
5.4	Experiments	55
5.4.1	All-optical modulation	56
5.4.2	Ultrafast signal detection	58
6.	Conclusions and outlook	61
	References	65
	Publications	73

List of Publications

This thesis consists of an overview and of the following publications which are referred to in the text by their Roman numerals.

- I** A. Shevchenko, M. Nyman, V. Kivijärvi, and M. Kaivola. Optical wave parameters for spatially dispersive and anisotropic nanomaterials. *Optics Express*, vol. 25, no. 8, 8550–8562, April 2017.
- II** M. Nyman, V. Kivijärvi, A. Shevchenko, and M. Kaivola. Generation of light in spatially dispersive materials. *Physical Review A*, vol. 95, 043802, April 2017.
- III** M. Nyman, A. Shevchenko, and M. Kaivola. Fluorescence enhancement and nonreciprocal transmission by nanomaterial interfaces. *Physical Review A*, vol. 96, 053828, November 2017.
- IV** M. Nyman, A. Shevchenko, I. Shavrin, Y. Ando, K. Lindfors, and M. Kaivola. Large-area enhancement of far-field fluorescence intensity using planar nanostructures. *APL Photonics*, vol. 4, 076101, July 2019.
- V** M. Nyman, S. Maurya, M. Kaivola, and A. Shevchenko. Optical wave retarder based on metal-nanostripe metamaterial. *Optics Letters*, vol. 44, no 12, 3102–3105, June 2019.
- VI** M. Nyman, M. Kaivola, and A. Shevchenko. All-optical modulation and detection using a gain medium in a pulse shaper. *Optics Express*, vol. 28, no 24, 35869–35883, 23 November 2020.

Author's Contribution

Publication I: “Optical wave parameters for spatially dispersive and anisotropic nanomaterials”

AS developed the theory with contribution from MN and VK. MN and AS designed the metamaterial used as a numerical example. MN performed the numerical calculations. AS wrote the manuscript with contribution from the other authors.

Publication II: “Generation of light in spatially dispersive materials”

MN developed the theoretical method. VK and AS designed the diffraction-compensating metamaterial and calculated its wave parameters. MN performed all other calculations. MN wrote the manuscript with contribution from the other authors. AS and MK supervised the work.

Publication III: “Fluorescence enhancement and nonreciprocal transmission by nanomaterial interfaces”

MN and AS developed the theory. MN performed the calculations. MN wrote the manuscript with contribution from the other authors. AS and MK supervised the work.

Publication IV: “Large-area enhancement of far-field fluorescence intensity using planar nanostructures”

MN developed the theory and designed the nanostructures, with input from AS. MN fabricated the flat-film samples and the planar metal-dielectric

resonator. IS, YA and KL fabricated the grating sample and a number of preliminary samples. MN built the experimental setup and characterized the samples, with advice from AS and KL. MN wrote the manuscript with contribution from the other authors. AS and MK supervised the work.

Publication V: “Optical wave retarder based on metal-nanostripe metamaterial”

MN designed the nanomaterial, developed the theoretical description and performed all calculations. SM developed the fabrication method together with AS. SM fabricated the sample and performed optical experiments. MN performed electron microscopy and focused ion beam milling. MN wrote the manuscript with contribution from the other authors. AS and MK supervised the work.

Publication VI: “All-optical modulation and detection using a gain medium in a pulse shaper”

MN developed the theoretical description. MN designed and built the experimental setup and performed all experiments with advice from AS. MN wrote the manuscript with contribution from the other authors. AS and MK supervised the work.

Other publications to which the author has contributed

- A. Shevchenko, P. Grahm, V. Kivijärvi, M. Nyman and M. Kaivola, “Spatially dispersive functional optical metamaterials”, *J. Nanophoton.* **9**, 093097 (2015).
- V. Kivijärvi, M. Nyman, A. Kärtilä, P. Grahm, A. Shevchenko and M. Kaivola, “Interaction of metamaterials with optical beams”, *New J. Phys.* **17**, 063019 (2015).
- V. Kivijärvi, M. Nyman, A. Shevchenko and M. Kaivola, “An optical metamaterial with simultaneously suppressed optical diffraction and surface reflection”, *J. Opt.* **18**, 035103 (2016).
- V. Kivijärvi, M. Nyman, A. Shevchenko and M. Kaivola, “Optical-image transfer through a diffraction-compensating metamaterial”, *Opt. Express* **24**, 9806–9815 (2016).
- V. Kivijärvi, M. Nyman, A. Shevchenko and M. Kaivola, “Theoretical description and design of nanomaterial slab waveguides: application to compensation of optical diffraction”, *Opt. Express* **26**, 9134–9147 (2018).
- E. Ilina, M. Nyman, I. Švagždýtė, N. Chekurov, M. Kaivola, T. Setälä, and A. Shevchenko, “Aberration-insensitive microscopy using optical field-correlation imaging”, *APL Photonics* **4**, 066102 (2019).
- S. Maurya, M. Nyman, M. Kaivola and A. Shevchenko, “Highly birefringent metamaterial structure as a tunable partial polarizer”, *Opt. Express* **27**, 27335–27344 (2019).
- E. Ilina, M. Nyman, T. Mondal, M. Kaivola, T. Setälä, and A. Shevchenko, “Interferometric imaging of reflective micro-objects in the presence of strong aberrations”, *Opt. Express* **28**, 1817 (2020).

Other publications to which the author has contributed

- S. Maurya, M. Nyman, M. Kaivola and A. Shevchenko, “Near-field spatial coherence of structures incoherent optical sources”, *Phys. Rev. A* **102**, 053509 (2020).
- A. Shevchenko, V. Vashistha, M. Nyman and M. Kaivola, “Electromagnetic anapoles of a Cartesian expansion of localized electric currents”, *Phys. Rev. Res.* **2**, 042043(R) (2020).

1. Introduction

Nanophotonics is the science and technology of controlling light with nanoscale structures and optical phenomena. The motivation for doing this is many-fold, but I wish to highlight two aspects that are very important in optical technology. The first motivation is miniaturization, that is, making smaller components and devices. The second motivation is controlling physical phenomena that can only be fully controlled at the nanoscale, such as the emission of light by molecules. Nanophotonics is therefore a field that one looks into when thinking of tomorrow's light sources, optical detectors, communications systems and optical data processors.

This dissertation is focused on three interrelated topics in the field of nanophotonics and, more generally, optics: artificial optical nanomaterials, the generation of light, and the control and modulation of light. These topics constitute a significant part of the flow of light in a nanophotonic device. For example, in an optical signal processor, light is generated, information is added to it by modulation, different signals modulate each other, and finally the result of the processing is detected or sent somewhere else. When we enhance and control these parts of the flow by nanostructures, we will have constructed a true nanophotonic signal processor.

1.1 Photonics and nanomaterials

The reason why artificial optical materials have to be structured at the nanoscale is that the material's structural units have to be smaller or at most about the same size as the wavelength of light. Wavelengths of the visible and near-infrared spectral domains range from about 400 nm to 2 μm , so nano-objects well below 1 μm in size are a necessity. The size of the structural units relative to the wavelength determines which "regime" of optics is the most important for a given structure. Starting from the structures that are typically the largest, photonic crystals are periodic arrays of dielectric constituents (often simply holes or spheres) that chiefly rely on diffraction to guide and control light [1]. The array period (lattice

constant) is therefore on the order of one half of a wavelength, which is where Bragg diffraction takes place. Moving to smaller sizes, optical metamaterials are (usually) periodic arrays of scatterers, typically made of metals or dielectrics, that form an *effective medium* for light. This means that, often, light propagates through a metamaterial as if it was a homogeneous material with extraordinary optical properties [2]; I will later discuss how this has important implications in the design and use of such materials. To act as an effective medium the array period of the material usually has to be smaller than half the wavelength, and in many cases, it is desired to make it as small as possible, less than one tenth of the wavelength [3, 4]. Finally, at the smallest size scale, quantum dots, wires and wells are structures typically made of semiconductor materials that have engineered electronic energy levels; this engineering leads to modified optical properties. Quantum confinement of the electrons is required for this, putting the size scale to 1 - 10 nm, by far smaller than the wavelength of light [5]. I note here that in other parts of the electromagnetic spectrum, for example in the microwave region, wavelengths can be far longer than in the optical region, and there the structural units of photonic crystals and metamaterials can be correspondingly larger. However, the properties of materials are usually very different in the optical and microwave regions. Therefore the same design of an artificial material does not always work in all regions of the spectrum. Out of the three regimes mentioned, this dissertation will concentrate on the second: the effective medium regime of optical metamaterials.

As I mentioned before, miniaturization is one of the key motivations for using nanomaterials and nanostructures in optics. For example, lasers, the smallest of which currently in common use are laser diodes, can be miniaturized, becoming nanolasers just a few hundred nanometres in size [6]. Such lasers can have low laser threshold and thus low power consumption. Beam steering devices, normally implemented using bulk lenses or mirrors, can instead be built from *metasurfaces* that are very thin and can more easily be integrated in flat optical systems [7, 8]. In the realm of photonic integrated circuits, nanomaterials have been used to construct components such as beam splitters and couplers with a smaller footprint than traditional waveguide-based methods would allow [9, 10].

The new and improved capabilities brought by nanostructures are another reason for scientific and technological interest in them. Metamaterials often exhibit optical properties that are not encountered in nature, such as negative refractive index, with associated applications, e.g., in super-resolution lenses [11, 12]. Metamaterials can also be engineered to have very strong anisotropy [13], chirality [14], and other properties that are usually very weak in traditional optical materials. Nanoantenna arrays can be used for sensitive chemical detectors based on fluorescence or surface-enhanced Raman scattering [15–17]. The efficiency of light

emitting diodes can be improved by making use of nanostructure-based output couplers [18–20]. Optical modulators relying on weak nonlinear effects such as two-photon absorption can be made more efficient with the help of nanoresonators and metasurfaces [21, 22].

The use of nanomaterials also presents challenges. Artificial nanostructures must be designed, which is not necessarily straightforward because light-matter interaction in such structures can be a complicated phenomenon. One must usually use full-wave numerical simulations, solving Maxwell’s equations in the desired structure, trying to optimize multiple parameters. This is a slow process, and does not always yield insight as to *why* a certain nanostructure works or does not work well. From an engineering point of view this knowledge is not always required as evidenced by some of the computer-optimized integrated-optics component designs mentioned earlier [9, 10]. However, it is essential from a physicist’s point of view, and can also shed light on engineering issues such as finding the ultimate limits of a given design and what could be done to exceed them. On the practical side, the fabrication of nanomaterials presents another challenge. Even when making only a surface structure with a single layer, one still desires fine resolution, arbitrary shapes and large area. Electron-beam lithography is the go-to solution for most research purposes but it is time-consuming for large-area devices. As such, alternative fabrication methods such as nanoimprinting and self-assembly are currently being studied and developed [23]. The fabrication of *three-dimensional* nanomaterials, consisting of many layers, is even more difficult [24]. Practical issues such as the fragility of many nanostructures, scattering and absorption losses, must also be considered.

In this dissertation I tackle the design problem for nanomaterials that control optical emission, specifically spontaneous emission by quantum emitters embedded within a metamaterial. I describe the optical properties of metamaterials with wave parameters, the effective refractive index and wave impedance that depend on the propagation direction. I then analyze optical emission by using an electric current decomposition to find out how a quantum emitter couples to each of the waves that can be excited in the metamaterial. Besides the work related to optical emission, I also discuss a particular application of optical nanomaterials in the form of a metal-dielectric metasurface wave plate that is used to control the polarization of light.

1.2 All-optical modulation and detection

Modulation is the act of including information in an optical signal. Normally the source of the modulation is an electrical signal, but in all-optical modulation, it is another optical signal. All-optical modulation is useful,

because it allows one to construct telecommunications systems and optical data processors that do not require interconversion between optical and electrical signals [25]. Such systems can exploit the large bandwidths available at optical frequencies at every point in the signal flow. Two examples of these broad bands are the 4-THz-wide near-infrared C-band provided by erbium doped fiber amplifiers [26] and the 330 THz band provided by a titanium-sapphire laser with a 3 fs pulse width. To make the contrast to electronics explicit, commonly-available fast electro-optic modulators and photodetectors operate at 10 GHz to 100 GHz speeds (as seen in manufacturer catalogs, e.g., in [27]). In systems where electrical-optical conversion is required, these speeds set the limit for single-channel bandwidth. As an example, the full optical bandwidth of 4 THz telecommunications band can only be accessed through wavelength division multiplexing. This technology is currently in use in the fiber-optic communications that form the backbone of the Internet, and increasingly, in shorter-distance communications [28]. An all-optical system could potentially use the full bandwidth on a single channel, dispensing with the need for spectral splitting and combining, as well as eliminate any delays due to electrical-optical conversion.

All-optical modulation, intriguing as it is, faces significant challenges. To make two optical signals interact, one must use nonlinear optics. From the bandwidth point of view, the best nonlinear optical effects to use are the fastest ones, chiefly, optical Kerr effect and two-photon absorption [29,30]. Unfortunately, these third-order nonlinear effects are also weak, in that a very large intensity of light (or a very long interaction length as in an optical fiber) is required to cause a significant effect on the other optical signal. This makes it difficult to achieve a significant modulation depth that is required for proper discrimination of different signal values, and requires significant power as well. On the other hand, effects with on-resonance transitions such as gain medium population changes can be stronger, but they cannot be used for fast modulation because it takes a long time (typically nanoseconds) for them to recover from an excitation [31,32].

Many researchers have taken the approach of strengthening the weak nonlinear effects by using resonators [21, 33], nanomaterials [22] and highly nonlinear waveguides [34,35]. This is fruitful, but the use of resonant elements also tends to narrow the bandwidth available. In this dissertation I present an alternative method to achieve high-speed all-optical modulation. It relies on using a strong but relatively slow effect, population changes in a gain medium, together with a pulse shaper that allows one to modulate different spectral components of the signal separately. Taken together, this spectrally-addressed modulation can be used to cause sub-picosecond changes in the signal. I also demonstrate a new way of detecting sub-picosecond signals that utilizes the pulse shaper device for its time-to-space mapping capabilities.

1.3 Structure of dissertation

This dissertation's compiling part is structured as follows. Chapter 2 describes the work on the properties of optical metamaterials (Publication I), and the theoretical work on optical emission in nanomaterials (Publication II and Publication III). Chapter 3 expands on the theory and introduces experimental results of optical emission enhancement by nanostructures (Publication IV). Chapter 4 is devoted to the design and experimental demonstration of a nanostructured optical wave plate (Publication V). Chapter 5 introduces the concept and theoretical and experimental demonstration of all-optical modulation and detection (Publication VI). Chapter 6 presents conclusions and ideas for future research.

2. Optical emission in nanomaterials

2.1 Metamaterials and spatial dispersion

In Chapter 1 I divided optical nanomaterials to three categories based on the size of their structural units relative to the optical wavelength λ : photonic crystals (about $\lambda/2$), metamaterials (about $\lambda/50 - \lambda/2$), and quantum-confined structures (below 10 nm; this is about $\lambda/50$ and less for visible light). In this section I concentrate on metamaterials. Due to the sub-wavelength size of the units, metamaterials do not exhibit diffractive wave-splitting effects at the wavelengths they are designed for. Usually, the idea of a metamaterial is that it acts as if it was a homogeneous medium with optical properties that are decided by the structure. This is interesting, because metamaterials can be constructed to exhibit properties that are not encountered in nature. A topic of especially intense study has been metamaterials with a negative index of refraction [11,12], with applications such as lenses with resolution exceeding the normal diffraction limit. Another very active research topic has been hyperbolic metamaterials, which cause a different type of negative refraction [13] and also have applications in the control of spontaneous emission [36–38]. There are many other examples of metamaterials as well, including zero-index or epsilon-near-zero metamaterials [39] and strongly chiral metamaterials [14].

To be precise, a metamaterial can be seen as an effectively homogeneous medium if, for each plane wave sent through the material, only one Bloch mode is excited [3,4]. Multiple Bloch modes usually start to propagate as soon as the metamaterial's lattice period exceeds $\lambda/2$, but they can also propagate in other situations such as when there is significant near-field coupling between the structural units [4]. Even when a metamaterial is homogenizable, it can still be considerably more complex to describe than an ordinary material consisting of molecular structural units. Molecules packed in a lattice with a very small period usually exhibit only electric-dipole excitations [40,41]. Metamaterial unit cells are sub-wavelength

but not deeply so, and as such they allow higher-order multipoles to be efficiently excited as well [42].

When only electric-dipole and magnetic-dipole excitations are significant, it is possible to describe a homogenizable metamaterial in the usual way, using electric permittivity and magnetic permeability tensors $\overleftrightarrow{\epsilon}$ and $\overleftrightarrow{\mu}$. In this case, one could simply determine the electric and magnetic fields \mathbf{E} and \mathbf{H} and the electric and magnetic flux densities \mathbf{D} and \mathbf{B} in the material, and then spatially average them over the unit cells, obtaining the constitutive relations $\mathbf{D} = \overleftrightarrow{\epsilon} \mathbf{E}$ and $\mathbf{B} = \overleftrightarrow{\mu} \mathbf{H}$ [41]. However, this approach is limited to small unit cells, and for such materials the magnetic dipole excitations tend to vanish [43], leaving only $\overleftrightarrow{\epsilon}$. In the presence of higher-order excitations, such as electric quadrupoles, these tensors begin to depend on the direction of propagation of light: the material exhibits *spatial dispersion*. There have been attempts to theoretically describe spatial dispersion and determine the appropriate characteristic quantities that describe a certain spatially dispersive material. Perhaps the most convenient way to do this is to use *wave parameters*, described in the next section.

2.2 Wave parameters

Instead of defining quantities that “globally” describe a material, wave parameters are defined for each plane wave direction and polarization in the metamaterial. In the following I discuss the wave parameters featured in Publication I. In the simplest case, when a material only has electric-dipole excitations only one wave parameter is needed for each plane wave: the effective refractive index n . When magnetic dipoles and electric quadrupoles are present, another independent parameter is required: the wave impedance Z . In spatially dispersive materials these parameters depend not only on light polarization and frequency, but also on the propagation direction, that is, the direction of the wave vector \mathbf{k} . All of this is somewhat true for ordinary anisotropic materials (described by an $\overleftrightarrow{\epsilon}$ tensor) as well, but in this case the actual \mathbf{k} -dependence is much more limited. For example, the isofrequency surface of n for non-spatially-dispersive materials can only be ellipsoidal or hyperboloidal, while for spatially dispersive materials it can be considerably different, ultimately limited by more fundamental considerations such as symmetries and optical reciprocity.

The wave parameters n and Z are not the only possible choice: at least \mathbf{k} -dependent scalar permittivity and permeability [44] and a \mathbf{k} -dependent permittivity tensor [45] have made their appearance in other works. However, n and Z are convenient and physically intuitive in many ways. The refractive index n of course describes the phase velocity and the wave-

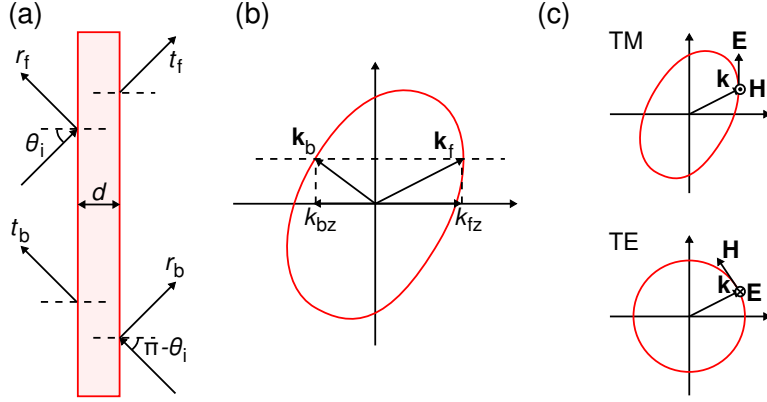


Figure 2.1. Calculating the wave parameters of a metamaterial. In (a), plane waves (k -vectors depicted by black arrows) propagate through a metamaterial slab (red) and the transmission and reflection coefficients are determined. (b) shows the material's k -surface (whose shape is the same as the isofrequency surface of the refractive index n) and wave vectors of the forward and backward waves (subscripts f and b , respectively) that were excited in (a). The horizontal dashed line denotes the k_x -component that is the same for all the plane waves, including those outside the metamaterial. In (c), the k -surfaces for TM and TE polarized waves are used to determine the directions of the electric and magnetic fields, such that the total impedance can be found.

length of a plane wave and thus tells us of how the wave propagates in the material, while the impedance Z describes the relationship between electric and magnetic fields, which determines the reflection and transmission at the interface between different materials. They can also be determined for a given material from the transmission and reflection coefficients of a slab of that material.

The method used in this dissertation to retrieve n and Z from transmission and reflection calculations is presented succinctly in Publication I. As depicted in Fig. 2.1(a), we take a slab of the material with thickness d , surrounded by an ambient, isotropic medium of refractive index n_s . Most conveniently, we can set the thickness d equal to the z -directional unit cell size of the material, so that in computations we need only consider one unit cell (along with periodic boundary conditions in the x - and y -directions). For the incidence angle θ_i we must determine four quantities. Two of them are the transmission and reflection coefficients of the slab, t_f and r_f , for the wave incident from the left-hand side. The other two are the transmission and reflection coefficients, t_b and r_b , for a wave incident from the right-hand side at the angle $\pi - \theta_i$. This accounts for the fact that as the wave incident from the left reflects back and forth between the two interfaces of the metamaterial, it “feels” the optical properties of the material in both directions: in general, these may be different. This is illustrated by the k -surface of Fig. 2.1(b) where waves that have the same k_x -component will have different k_z -components when travelling in the forward and backward

directions (waves k_f and k_b , respectively).

The method relies on the fact that, in this geometry, if the metamaterial has a certain refractive index and impedance for the forward and backward-propagating waves, then the transmission and reflection coefficients of the ambient-metamaterial interfaces (generalized Fresnel coefficients) can be determined. Furthermore, the transmission and reflection coefficients of the slab can be calculated by following the multiple reflections of a wave propagating through the slab. We can now proceed in the inverse direction: knowing the transmission and reflection coefficients, we solve the Fabry-Perot equations to yield n and Z . To be more accurate, we first obtain the z -directional component of the wave vector and the normalized *tangential impedance* ξ in both the forward and backward directions, through the equations

$$k_{fz} = [-i \ln(a \pm \sqrt{a^2 - b}) + 2\pi m]/d, \quad (2.1)$$

$$\xi_{f,\parallel} = \frac{1 - t_f \exp(ik_{bz}d) + r_f}{1 - t_f \exp(ik_{bz}d) - r_f}, \quad (2.2)$$

$$k_{bz} = [i \ln(a \mp \sqrt{a^2 - b}) + 2\pi m]/d, \quad (2.3)$$

$$\xi_{b,\parallel} = \frac{1 - t_b \exp(ik_{fz}d) + r_b}{1 - t_b \exp(ik_{fz}d) - r_b}, \quad (2.4)$$

where

$$a = \frac{1 + t_f t_b - r_f r_b}{2t_f}, \quad (2.5)$$

$$b = \frac{t_b}{t_f}. \quad (2.6)$$

We then obtain the refractive indices of the forward and backward waves from

$$n_f = \sqrt{k_{\parallel}^2 + k_{z,f}^2}/k_0, \quad n_b = \sqrt{k_{\parallel}^2 + k_{z,b}^2}/k_0, \quad (2.7)$$

where k_0 is the wavenumber in vacuum and $k_{\parallel}^2 = k_x^2 + k_y^2$. The impedance is slightly more complicated. The tangential impedance determined above gives only the relationship between the electric and magnetic field components that are tangential to the surface of the material. Therefore, the x - and y -components of the fields are determined, but not the z -components. To determine these, one needs to consider the shape of the k -surface (or, equivalently, the isofrequency surface of n) as shown in Fig. 2.1(c). Like in ordinary anisotropic materials, the electric and magnetic fields are tangential to this surface, and knowing their vector directions and the x - and y -components of the fields, the z -components of the fields can be determined (see Eqs. (25)–(30) in Publication I). It is useful to note that if one is interested only in the fields outside the metamaterial slab, then the

tangential impedances have enough information and it is not necessary to determine the full impedance.

Once the wave parameters have been determined, more complex problems than just plane-wave propagation can be also solved. I will apply this to optical emission in the next section, but at first, let us consider the propagation of an arbitrary optical beam in a metamaterial. Any electromagnetic field can be seen as a superposition of plane waves. Mathematically, if the field of a beam is known on the xy -plane at $z = 0$ (I call this the input plane), the plane-wave amplitudes are obtained from the following Fourier transform: [46]

$$\hat{\mathbf{E}}(k_x, k_y) = \iint \mathbf{E}(x, y; 0) e^{-i(k_x x + k_y y)} dx dy, \quad (2.8)$$

where $\hat{\mathbf{E}}(k_x, k_y)$ is the angular spectrum of the field, k_x and k_y are the x - and y -components of the wave vector, and $\mathbf{E}(x, y; 0)$ is the field on the input plane. To find the angular spectrum at some other z -coordinate, we multiply it by the plane-wave propagator $\exp[ik_z(k_x, k_y)z]$, where $k_z(k_x, k_y)$ is the z -component of the wave vector and can be obtained from

$$k_z(k_x, k_y) = \sqrt{k_0^2 n(k_x, k_y)^2 - k_x^2 - k_y^2}, \quad (2.9)$$

where $n(k_x, k_y)$ is the isofrequency contour of the refractive index in terms of $k_x = k_0 n(\theta, \phi) \sin \theta \cos \phi$ and $k_y = k_0 n(\theta, \phi) \sin \theta \sin \phi$. The field at this output plane is therefore obtained from the inverse Fourier transform as

$$\mathbf{E}(x, y, z) = \iint \hat{\mathbf{E}}(k_x, k_y) e^{ik_z(k_x, k_y)z} e^{i(k_x x + k_y y)} dk_x dk_y. \quad (2.10)$$

2.3 Optical emission

Spontaneous emission takes place when a quantum emitter, for example a molecule, is in an excited state and decays to a lower state by emitting a photon. There are two contributors to this process: the internal properties of the emitter and the coupling into the electromagnetic environment. Together these determine the rate, spectrum, and radiation pattern of the emission [47].

Briefly, from the quantum mechanical point of view, an optical transition happens when the excited state and the lower state are coupled by the electric field of an electromagnetic mode. Even in the vacuum state, the mode exhibits so-called vacuum fluctuations: i.e., a randomly changing electric field. This fluctuation can induce the spontaneous emission process, in which energy from the emitter is transferred into the electromagnetic mode. Most commonly, the photon is lost from the electromagnetic mode quickly, either by absorption by other quantum systems or by radiation into

infinite space (that is highly multimodal). In this case, the emitter is in the *weak coupling* regime, and spontaneous emission is more or less an irreversible process (the mathematical formulation of spontaneous emission in the weak coupling regime falls under the so-called Weisskopf-Wigner approximation [48]). The reverse process, the photon being absorbed back into the emitter, is only possible in the case of *strong coupling* between the emitter and the electromagnetic mode this happens. This usually requires the mode to have very low losses and a small mode volume, conditions mostly fulfilled in high-quality-factor microcavity resonators [49]. Strong coupling leads to Rabi oscillations where the excitation transfers back and forth between the emitter and the mode. Equivalently, we may understand this situation as one where the emitter and the electromagnetic environment are no longer separate entities, but instead a hybrid which has new types of energy states (the corresponding photon-emitter quasiparticle is then termed a cavity polariton [50]). In this dissertation we concentrate on the weak coupling regime.

Here I also note that most optical transitions in atoms and molecules are dipole transitions: they couple to electromagnetic modes that have a constant electric-field strength over the extent of the quantum emitter. Higher-order transitions (quadrupole etc.) are less common for small particles because they couple to electromagnetic modes with spatially varying electric-field strength. Because atoms, molecules and quantum dots are very small compared to the emission wavelength, this variation is slight, and the coupling very weak [51].

With the Weisskopf-Wigner and dipole approximations in one hand and Maxwell's equations in the other, one can find out how exactly an optical transition couples into the electromagnetic modes of, say, a nanostructure, in a rather straightforward manner. One simply replaces the quantum emitter with an oscillating electric dipole and uses Maxwell's equations to calculate the electromagnetic field created by the dipole. This field is the superposition of all the electromagnetic modes that the dipole excites. Knowing this, one can find, e.g., the radiation pattern, the time-dependent behaviour of the emitter itself [52], and the coupling coefficients between the emitter and the modes if required. I will further simplify this picture in Chapter 3 to address the impact of modified spontaneous emission on such parameters as emission rate and quantum yield. In this chapter, I will concentrate on the classical electromagnetic part, that is, finding the electromagnetic field radiated by the electric dipole.

The problem of dipole emission can be solved analytically in a homogeneous medium [53–55] and layered media through the use of transfer-matrix methods [56, 57]. In the presence of nanostructures, exact results can usually only be obtained using full-wave numerical calculations using, e.g., the finite-difference time-domain method or the finite element method. Emission in photonic crystals can also be analyzed using Bloch modes [58]

which can be determined using various methods [1]. Metamaterials are an interesting case: on one hand, they can be seen as effectively homogeneous media, but on the other, the near fields of a metamaterial's nanostructure affect the dipole emission depending on where exactly in the unit cell the dipole is located. It turns out that the effectively homogeneous picture can still be remarkably accurate, but this requires a proper treatment of spatial dispersion. The wave parameters, combined with an electric-current decomposition method presented in Publication II, provide this treatment.

2.4 Electric-current decomposition method

Let us assume that we have a spatially dispersive metamaterial and are interested in the electromagnetic field created by an embedded electric dipole oscillating at frequency f . First, we determine the wave parameters n and Z for all relevant plane waves, obtaining the isofrequency surfaces $n = n(\theta, \phi)$ and $Z = Z(\theta, \phi)$. Here, the spherical coordinate angles θ and ϕ give the direction of the wave vector, $\hat{\mathbf{k}} = \hat{\mathbf{x}} \sin \theta \cos \phi + \hat{\mathbf{y}} \sin \theta \sin \phi + \hat{\mathbf{z}} \cos \theta$. These surfaces can be different for different polarizations.

As explained in section 2.2, the field created by the dipole can be expressed as a superposition of plane waves. The problem is then to determine the amplitudes of these plane waves. One does this by first expanding the *electric current distribution* of the dipole in planar waves of electric current. This is done with the same kind of Fourier transform as was used for expanding the electric field of a beam of light (Eq. (2.8)), but replacing the electric field with the electric current:

$$\hat{\mathbf{K}}(k_x, k_y) = \iint \mathbf{K}(x, y) e^{-i(k_x x + k_y y)} dx dy, \quad (2.11)$$

where $\hat{\mathbf{K}}(k_x, k_y)$ is the spatial spectrum of the surface current density $\mathbf{K}(x, y)$. A dipole at $x = 0, y = 0$ has $\mathbf{K}(x, y) = \mathbf{K}_0 \delta(x, y)$, where $\delta(x, y)$ is the Dirac delta function and \mathbf{K}_0 is the electric-current amplitude of the dipole, related to the dipole moment \mathbf{p} through $\mathbf{K}_0 = -i\omega \mathbf{p}$. As such, the spatial spectrum is $\hat{\mathbf{K}}(k_x, k_y) = \mathbf{K}_0$ for a dipole: all electric-current waves are excited equally. We also note that unlike for electromagnetic plane waves, there is no z -component for the electric-current wave vector. For convenience, we can define the transverse wave vector for the current as $\mathbf{k}_{\text{tr}} = \hat{\mathbf{x}} k_x + \hat{\mathbf{y}} k_y$.

Each of the electric-current waves emits two plane waves (see Fig. 2.2): one to the left and another to the right (negative and positive z -directions, respectively). We must now use the electromagnetic boundary conditions to derive the electric field amplitude of the plane waves. The derivation is presented in Publication II in more detail. Here, we note that an electric-current wave with the transverse wave vector \mathbf{k}_{tr} generates electromagnetic plane waves which have the same k_x and k_y . We must

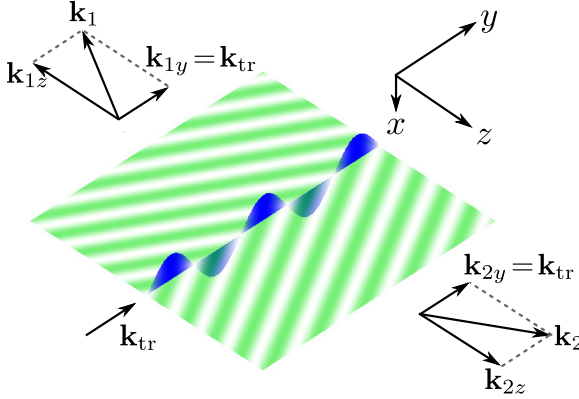


Figure 2.2. Emission of optical plane waves (green) by a planar (in the xy -plane) electric-current wave (blue). The wave vector components in the xy -plane are matched due to electromagnetic boundary conditions.

also consider three cases based on the direction of the electric current and the wave direction. The first is when \mathbf{K}_0 is perpendicular to \mathbf{k}_{tr} . In this case, transverse electric waves are generated. The second case is when \mathbf{K}_0 is parallel to \mathbf{k}_{tr} , which leads to the generation of transverse magnetic waves. The third case has a z -directional \mathbf{K}_0 : this also generates transverse magnetic waves but with a different amplitude. For simplicity, we can set the coordinate system such that $\mathbf{k}_{tr} = yk_y$. The following equations give the electric-field amplitudes of the plane waves emitted to the positive z -direction in each of the three cases discussed above (see Publication II):

$$E_x = - \left(-\frac{k_{1z}}{k_0 n_1 \eta_1} + \frac{k_{2z}}{k_0 n_2 \eta_2} \right)^{-1} K_{0x} \quad (2.12)$$

$$E_y = - \left(-\frac{k_0 n_1}{k_{1z} \eta_1} + \frac{k_0 n_2}{k_{2z} \eta_2} \right)^{-1} K_{0y} \quad (2.13)$$

$$E_z = \left(1 - \frac{k_{1z} \eta_1 n_2}{k_{2z} \eta_2 n_1} \right)^{-1} \left(\frac{\eta_1}{n_1} + \frac{\eta_2}{n_2} \right) \frac{k_y}{2k_0} K_{0z}. \quad (2.14)$$

The electric-field amplitudes of the generated plane waves make up the angular spectrum $\hat{\mathbf{E}}(k_x, k_y)$. To find the electric field anywhere in the material, we apply the inverse Fourier transform of Eq. (2.10).

We verified the correctness of the electric-current decomposition method by comparing its results to analytical results obtained for a known case (a dipole emitter in a uniaxial anisotropic material). However, the true strength of the method lies in analyzing optical emission in metamaterials. It has two key advantages over performing full-wave numerical simulations to model the emission. The first advantage is its speed: in general, large computational domains spanning many unit cells are required to properly analyze emission in metamaterials. This leads to a very heavy calculation. The electric-current decomposition method, on the other hand,

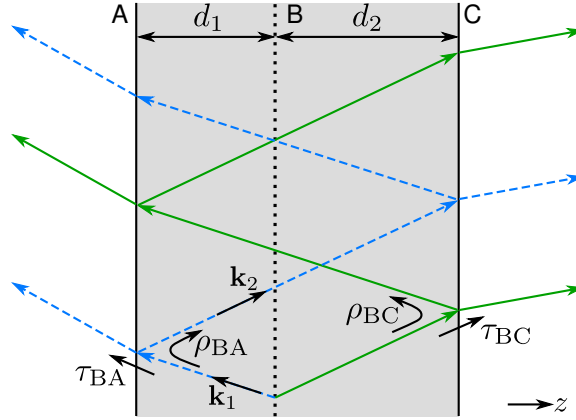


Figure 2.3. The escape of plane waves emitted by a planar electric-current source (dashed line) from a metamaterial slab (medium B) into the surrounding media (A and C). The waves initially emitted to the left and to the right are shown with dashed blue and solid green lines, respectively.

can easily handle computational regions hundreds of wavelengths in size. The retrieval of wave parameters still requires full-wave simulations, but these are single-unit-cell simulations which are comparatively easier. The second advantage is that with analytical equations it is easier to understand which parameter affects which aspect of the phenomenon, thus facilitating theoretical analysis and design.

2.5 Outcoupling of emission

In most applications such as light sources and chemical sensors, the light emitted from within the material must usually escape to a surrounding medium for it to be seen or detected, and so the outcoupling of emission is an important consideration. The electric-current decomposition method provides the electric-field amplitudes of the plane waves created by the dipole emitter. To find the field outside of a slab of the material, we can apply a model in which each emitted plane wave propagates to an interface of the material, is partially transmitted and reflected, and the subsequent multiple reflections are tracked in the same way as when deriving the transmission and reflection coefficients of a Fabry-Perot cavity [32, 59]. Figure 2.3 illustrates this method for one of the plane-wave components: the dotted line inside medium B is the planar electric-current sheet that emits left- and right-going waves (dashed blue and solid green lines, respectively). The media A and C are the ambient media on the left- and right-hand sides, and the transmission and reflection coefficients at the interfaces are given by the generalized Fresnel coefficients τ_{BA} , τ_{BC} , ρ_{BA} and ρ_{BC} (see Publication I and [46]). The source is located at a

distance d_1 from the BA-interface and distance d_2 from the BC-interface. The amplitudes of the waves emitted into media A and C (left and right) are given by the equations

$$\tilde{E}_L = \tau_{BA} e^{ik_{1z}d_1} \frac{\tilde{E}_1 + \rho_{BC} e^{i(k_{1z}+k_{2z})d_2} \tilde{E}_2}{1 - \rho_{BA}\rho_{BC} e^{i(k_{1z}+k_{2z})(d_1+d_2)}} \quad (2.15)$$

$$\tilde{E}_R = \tau_{BC} e^{ik_{2z}d_2} \frac{\tilde{E}_2 + \rho_{BA} e^{i(k_{1z}+k_{2z})d_1} \tilde{E}_1}{1 - \rho_{BA}\rho_{BC} e^{i(k_{1z}+k_{2z})(d_1+d_2)}}, \quad (2.16)$$

where \tilde{E}_1 and \tilde{E}_2 are the amplitudes of the plane waves emitted by the source as obtained from Eqs. (2.12)–(2.14).

In the case of a semi-infinite medium, the equations still apply, but this situation has an interesting caveat regarding the transmission out of the medium. Many metamaterials (chiefly plasmonic ones built from metal nanoparticles) are absorbing. In normal circumstances, absorption is detrimental to optical emission because it reduces the amount of emitted energy that can be exploited. Furthermore, absorption complicates the description of the energy flow inside metamaterials. In absorbing materials the intensity transmission coefficients of the interfaces, in the direction from inside the material to outside, can be larger than unity [60]. While this can seem to violate energy conservation, it actually does not, as we explored in Publication III.

Firstly, the paradox disappears when we recognize that it is the overall power flow (Poynting vector of the total field) that must be continuous across the interface to satisfy energy conservation. The power flow is described by the normal component of the time-averaged Poynting vector $S = 1/2\text{Re}\{\mathbf{E} \times \mathbf{H}^*\}$. In this case, the Poynting vector at the interface is not just $S = S_{\text{inc}} - S_{\text{ref}}$ like in non-absorbing media (here S_{inc} and S_{ref} are the Poynting vectors associated solely with the incident and reflected waves, respectively). The reason for this is that the incident and reflected waves interfere with each other, which produces a standing wave, which in turn in an absorbing medium produces a spatially-varying power absorption density. The Poynting vector then varies too: depending on the phase of the reflection coefficient of the interface, there might be a maximum or minimum of S at the interface. This is clearly seen from the following equation, which shows the normal component of the Poynting vector inside the medium with the interface located at $z = 0$:

$$S_{1,z} = \frac{|E_{\text{inc}}|^2}{2|\eta_1|^2} \{\text{Re}\{\eta_1\} [e^{-2\alpha_1 z} - |\rho_{12}|^2 e^{2\alpha_1 z} - 2\text{Im}\{\eta_1\} |\rho_{12}| \sin(2\beta_1 z + \phi)]\}. \quad (2.17)$$

Here, η_1 is the tangential impedance for the incident wave in the medium, α_1 is the absorption coefficient, ρ_{12} is the reflection coefficient of the interface, ϕ is its phase, and β_1 is the real part of the z-component of the wave vector of the incident wave. Notably, when the impedance is real, the usual situation prevails where no standing wave is visible in the Poynting vector

distribution. When there is an imaginary part, the interference starts to affect the result.

Secondly, when considering that the wave is generated by a source, we find that the emission power coupled through the interface can be enhanced. Considering a source that emits a single normal-incidence plane wave, with amplitude given by Eq. (2.12), the normal component of the Poynting vector just outside the interface in medium 2 is

$$S_2 = \frac{1}{2} \frac{1}{\eta_2} \left| \frac{1}{\eta_1} + \frac{1}{\eta_2} \right|^{-2} |K_0|^2 e^{-2\alpha_1 d} \quad (2.18)$$

where η_2 is the impedance of the second medium, K_0 is the electric-current amplitude of the source and d is the distance between the source and the interface. If one compares this result to the power flow that would be created by the same emitter in homogeneous glass (in absence of the interface), one can show that the wave's intensity can be enhanced by a factor of 4 at most. Interestingly, the same maximal enhancement is obtained when a source is placed in front of a perfectly-reflecting mirror at an optimal distance.

It follows that, counterintuitively, emission may still be efficiently coupled out of materials that are highly absorbing. The interference effect is responsible for this: if the Poynting vector of Eq. (2.17) is maximized at the interface, more power is coupled out. An example of this is given in the next section. The emission can even be *enhanced* because of this effect, and taking it into consideration may be helpful in the design of, e.g., fluorescence-enhancing metamaterials. Though here we have analyzed the situation from the point of view of one plane wave only, the electric-current decomposition method would allow doing so for the full angular spectrum of the emitter as well.

2.6 Examples

2.6.1 Diffraction-compensating metamaterial

Diffraction-compensating metamaterials utilize anisotropy and spatial dispersion to guide light in a special way: the propagation of optical power is allowed only in one direction [61–63]. Consider a material that has an effective refractive index described by

$$n = \frac{n_0}{\cos \theta}, \quad (2.19)$$

where n_0 is the refractive index at normal incidence. Plane waves entering this material will have a z -component of the wave vector equal to $k_z = k_0 n \cos \theta = k_0 n_0$, that is, the same for all angles θ . In Eq. (2.10) this

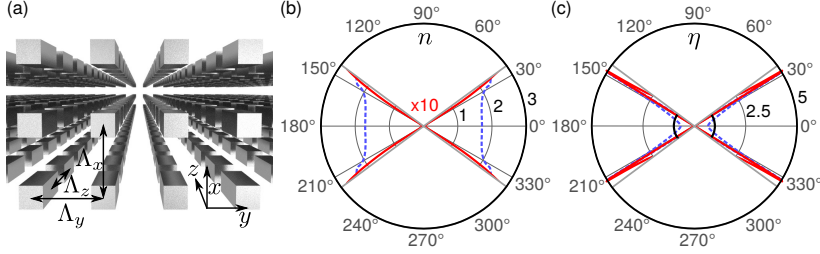


Figure 2.4. (a) The structure of a diffraction-compensating metamaterial composed of silver nanorods in a glass host medium. (b) The isofrequency contour of the refractive index n for TM-polarized waves. The dashed blue line and red solid line show the real and imaginary parts, respectively; the imaginary part has been multiplied by 10 to make it more visible. (c) The impedance (relative to the impedance of vacuum). The black line shows the impedance of glass. In (b) and (c), the white sectors centered at 90° and 270° correspond to waves that experience total internal reflection.

makes the factor $\exp[ik_z(k_x, k_y)z]$ a constant phase factor. Consequently, it does not influence the transverse intensity distribution of the propagating optical beam. As such, for example, a Gaussian beam focused on the surface of the metamaterial will stay focused as it propagates through the material and diverges only when it exits it again. As the isofrequency surface described by Eq. (2.19) is a flat line, spatial dispersion is clearly required to make it.

From the point of view of light sources this is an interesting phenomenon too: emitted optical energy will also be confined to narrow beams inside the material. To show this we took an earlier design of a diffraction-compensating metamaterial [61], shown in Fig. 2.4(a). This material consists of a lattice of silver nanorods set in glass. The rods are 40 nm wide and 130 nm long, while the lattice periods are 120 nm in the x - and y -directions and 200 nm in the z -direction. The material is designed for the wavelength 790 nm, which makes the unit cells about $\lambda/2.6$ in size. Spatial dispersion is therefore significant, and this is also witnessed in the isofrequency contours of the wave parameters. Figure 2.4(b) shows the refractive index, the real part of which closely follows Eq. (2.19) (a straight line in the polar plot). Another thing to note about the material is that the imaginary part of the refractive index (red curve) is small, signifying low absorption losses despite the material being made of plasmonic nanoparticles. Finally, the wave impedance shown in Eq. 2.4(c) is closely matched to the impedance of glass at normal incidence, which makes the interface between the metamaterial and glass non-reflective. Being able to tune the wave impedance separately from the refractive index is a great advantage brought about by judicious use of spatial dispersion.

To discuss first the “microscopic” picture of what happens to optical emitters inside the material, Fig. 2.5(a) shows the intensity distribution created by a dipole at the position of the black dot, inside a 8-unit-cells-

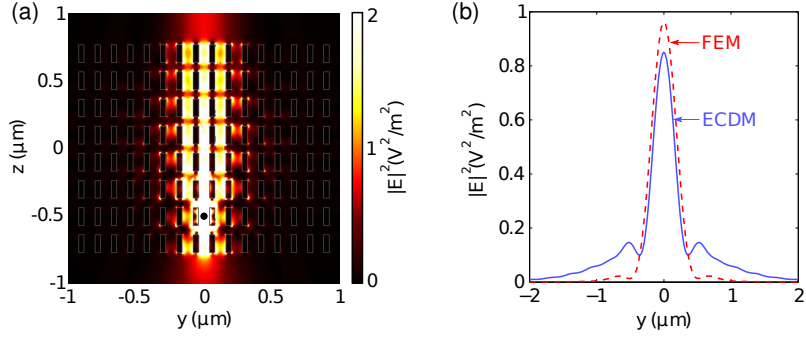


Figure 2.5. (a) The intensity distribution of the field generated by an oscillating dipole (position shown by the black dot) inside a diffraction-compensating metamaterial. The silver nanorods are shown as grey rectangles. (b) The intensity distribution just outside of the upper interface of the metamaterial, as calculated by the full-wave finite-element method and the electric-current decomposition method.

thick slab of the metamaterial. Full 3D calculations are very challenging in such large domains, so instead, we only took one layer of the metamaterial (the one seen in the picture) and used periodic boundary conditions to make the structure infinite in the x -direction. This also makes the dipole not just a single emitter, but instead a chain of coherently-oscillating dipoles. However, this simulation shows the salient behaviour of the optical emission: instead of spreading out in every direction like it normally would, all emitted power is confined in a narrow beam that propagates through the material and begins to diverge only after coming out.

Moving on to the effectively homogeneous medium picture, we used the electric-current decomposition method to calculate the intensity distribution at the output side of the slab and compared it to the finite-element calculation. The comparison is seen in Fig. 2.5(b), and shows how close the results are to each other. This demonstrates that the electric-current decomposition method can be used to predict optical emission characteristics to surprisingly high accuracy even in plasmonic metamaterials.

2.6.2 Metal-dielectric stack

To showcase the effect that Poynting-vector interference has on optical emission out of highly-absorbing metamaterials (analyzed in Publication III), I consider a simple metamaterial made of alternating thin films of silver and glass, depicted in Fig. 2.6(a). Materials such as this are often used as hyperbolic metamaterials that are described by a permittivity tensor with at least one positive and one negative element on the diagonal [13]. They receive their name from their hyperboloid-shaped isofrequency surfaces: the refractive index for the extraordinary wave grows as a function of propagation angle. Hyperbolic metamaterials allow an optical emit-

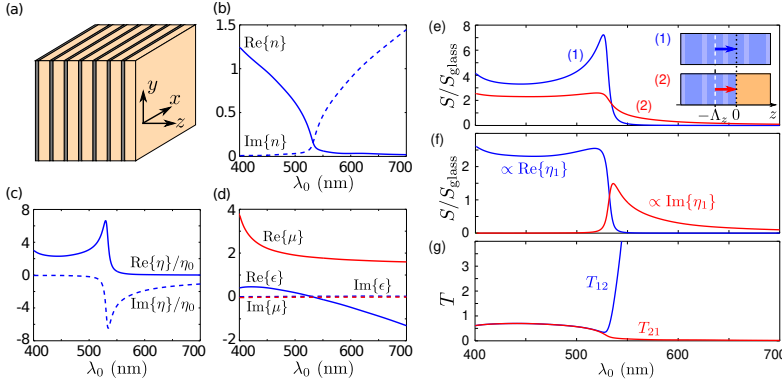


Figure 2.6. (a) Structure of a metal-dielectric stack metamaterial made of alternating layers of silver (gray) and glass (orange). (b) Refractive index at normal incidence. (c) Wave impedance at normal incidence. (d) Effective permittivity and permeability at normal incidence. (e) Case (1): Poynting vector in an infinite metamaterial, one unit cell away from the source. Case (2): Poynting vector at the interface between the metamaterial and glass, originating from a plane-wave emitter at one unit cell distance from the interface. (f) Contributions to the case (2) Poynting vector from the real and imaginary parts from the two terms of Eq. (2.17). (g) Intensity transmission coefficients at normal incidence from the metamaterial to glass (T_{12}) and in the reverse direction (T_{21}).

ter to radiate into these high-angle waves, which substantially changes the overall radiation rate [36–38]. The material analyzed in this section also acts as a hyperbolic metamaterial in a certain spectral range, but for clarity the consideration to normal incidence and thus the emission modification due to the extraordinary hyperbolic property is not analyzed. Figures 2.6(b) and 2.6(c) show the wave parameters at normal incidence as functions of wavelength. The material is absorptive throughout the spectrum (refractive index is complex-valued), and above the wavelength 530 nm it also reflects light substantially (impedance is very mismatched from vacuum or glass).

Figure 2.6(g) shows that, as discussed in section 2.5, the transmission coefficient T_{12} is larger than unity in the region where the imaginary part of the impedance has a large value. We now consider an emitter with only one electric-current sheet, generating normal-incidence plane waves. Case (2) of the inset of Fig. 2.6(e) shows that it is positioned inside the metamaterial, one unit cell from the material’s interface with homogeneous glass. The red curve of Fig. 2.6(e) shows the Poynting vector at the interface, relative to the Poynting vector that would be created if the same emitter was inside homogeneous glass. For example, at 538.5 nm (discussed in Publication III) the power flow is about 1.5 times higher, despite the radiation source being inside the non-transparent metamaterial. This is a clear sign of the interference-induced transparency effect that we set out to demonstrate.

For the sake of clarity, one should note here that the *attenuation* of waves is not necessarily equal to *absorption*. A material can be non-transparent

without any power loss involved, as exemplified by photonic crystals at the Bragg reflection induced band gap, or by an idealized metal having a purely real, negative permittivity ϵ . For such a material the effective refractive index is either purely real (transparent regime) or purely imaginary (non-transparent regime). Poynting's theorem can be used to show that power losses are proportional to the imaginary parts of ϵ and μ [64, 65]. Indeed, for the material of Fig. 2.6(a), these parameters are quite small as shown in Fig. 2.6(d). However, close to the plasma frequency at $\lambda = 530$ nm, the real and imaginary parts of ϵ are on the same order of magnitude, and thus absorption plays a large role in the material's optical response.

3. Large-area fluorescence enhancement

In Chapter 2 I concentrated only on one aspect of spontaneous emission modification, that being the determination of the electric-field distribution. By controlling the distribution one controls the radiation pattern of the emission. This is important when designing, e.g., light sources that must emit light in a certain cone, as well as in light-emitting diodes where the trapping of the optical radiation inside a diode's semiconductor is a problem. However, other factors must be considered as well: the modification of the total emission rate, known as the Purcell effect [66], and the enhancement (or reduction) of the excitation rate. In this chapter I take all of these effects into account in order to design nanostructures that enhance *fluorescence*, that is, spontaneous emission following optical excitation (pumping).

I mentioned in Chapter 2 that one should determine the coupling coefficients between a dipolar emitter and the electromagnetic modes in order to analyze the modified spontaneous emission. Here I will chiefly speak of *emission rates* into the modes, to which the coupling coefficients are of course related (see, e.g., Ch. 6.2 of [48]). I also note that most of the quantities discussed here are normally wavelength-dependent. When taken together with emitters that have broad spectra (such as fluorescent dyes and quantum dots), the emission spectrum is often substantially reshaped. I adopt a rather phenomenological approach where all quantities are determined wavelength-by-wavelength and no correlation between the different parts of the spectrum is assumed. This corresponds to inhomogeneous spectral broadening, where emitters are distributed in “classes” that each have a different central wavelength but a relatively narrow-band homogeneously-broadened emission spectrum [31]. We used fluorescent dyes in the experiments described at the end of this chapter; emitters of this type indeed have a narrow *homogeneous* lineshape but a wide total spectrum [67].

3.1 Factors that influence fluorescence enhancement

Consider a chemical sensor or a light source based on fluorescence, that is, optically-pumped spontaneous emission by (usually) organic molecules. One molecule is excited at a rate γ_{exc} , and emits a photon with probability η , known as the quantum yield. The photon is detected with a probability $\eta\gamma_{\text{ff}}/\gamma_{\text{tot}}$, where γ_{ff} is the emission rate into those far-field modes that are detected (e.g., those within the collection cone of a microscope objective) and γ_{tot} is the total emission rate into all modes. The rate of photons detected is therefore

$$\gamma = \eta \frac{\gamma_{\text{ff}}}{\gamma_{\text{tot}}} \gamma_{\text{exc}}, \quad (3.1)$$

and is seen to consist of three factors that can be enhanced by a nanostructure: the quantum yield η , the fraction of photons detected $\gamma_{\text{ff}}/\gamma_{\text{tot}}$, and the excitation rate γ_{exc} .

To find out how much a certain nanostructure enhances this rate, I introduce the fluorescence enhancement factor $F = \gamma/\gamma_0$, where γ_0 is the rate of photons detected in the absence of any structure. In Publication IV I split this into two parts as follows:

$$F = F_e F_p, \quad (3.2)$$

where F_e is an emission enhancement factor and F_p is an excitation enhancement factor (subscript p for “pumping”). The emission enhancement factor is

$$F_e = \frac{\gamma_{\text{ff}}}{\gamma_{\text{ff},0}} \frac{1 + \Gamma}{\mathcal{P} + \Gamma}, \quad (3.3)$$

where the quantities with subscript 0 pertain to the case of no structure. $\Gamma = \gamma_{\text{nr}}/\gamma_{\text{tot},0}$ is the ratio of the non-radiative and radiative decay rates, related to the intrinsic quantum yield by $\gamma = 1/\eta_{\text{intrinsic}} - 1$, and \mathcal{P} is the Purcell factor (the symbol P is used for it in Publication IV). The Purcell factor is defined as $\mathcal{P} = \gamma_{\text{tot}}/\gamma_{\text{tot},0}$.

Purcell enhancement is sometimes a goal in itself, for example when the objective is to make an emitter that can be modulated fast [68] and thus requiring the molecules to emit as soon as possible after being excited. Purcell enhancement also helps when trying to improve the quantum yield of the emitter [69]. It is, however, seen here that this does not necessarily help in enhancing the rate of the detected photons. This is because Purcell enhancement takes into account *all* of the emission, not just the part that is detected. A pathological case of this is the quenching of spontaneous emission in the presence of metal interfaces, where \mathcal{P} is massively increased but all the emitted photons are transferred through near fields into the metal where they are absorbed. Thus, if \mathcal{P} is enhanced without also enhancing $\gamma_{\text{ff}}/\gamma_{\text{ff},0}$, the emission enhancement factor decreases.

Another common case, sometimes seen when nanoparticles are used as optical antennas, is when \mathcal{P} is increased and $\gamma_{\text{ff}}/\gamma_{\text{ff},0}$ is increased in

proportion to it. This happens when the nanoantenna does not provide a large increase in the directivity of the radiation, but only in the emission rate. Then, F_e remains constant, except in the case of emitters with low quantum yields (large Γ) where Purcell enhancement actually improves the quantum yield [70].

The excitation enhancement factor F_p depends chiefly on the enhancement of the optical intensity of the pump light: $F_p = I_p/I_{p,0}$. It is important to note that the pump light almost always has a different wavelength from the emission. As such, to obtain the maximum possible brightness of the emission (that is, to maximize both F_e and F_p), one must design the structure to work properly for both the fluorescence and pump wavelengths.

The fluorescence enhancement factor F is a function of the position inside the nanostructure. For example, in the presence of a bowtie nanoantenna [70], significant enhancement takes place when the emitting molecule is at the “hot-spot” of one of the antennas, that is, the location of the maximum field enhancement. Outside the hot-spots, F may be smaller. To find out the overall fluorescence enhancement, it is therefore necessary to find the average F over the entire structure,

$$F_{\text{avg}} = 1/V \int \langle F(\mathbf{r}) \rangle d\mathbf{r}, \quad (3.4)$$

where V is the volume of one unit cell, the integration is performed over the unit cell, and the brackets $\langle \rangle$ denote averaging over all orientations of the emitter.

3.2 Calculations

I point out here that the methods described below are geared towards analyzing fluorescence enhancement in *periodic* nanostructures. Randomly positioned or single scatterers can be treated using the same approach, but they do not allow the use of periodic boundary conditions which otherwise simplify and speed up the numerical calculations significantly.

3.2.1 Directionality enhancement

To learn how a nanostructure modifies the fraction of photons detected $\gamma_{\text{ff}}/\gamma_{\text{ff},0}$, one generally has to determine the radiation pattern of an emitter at each position in the structure, and pick out the radiation that is supposed to be detected. As outlined in Chapter 2 this requires a numerical simulation of the dipole emission. When the outcoupled far field is of interest, this calculation can be simplified by using the Lorentz reciprocity principle [71]. The principle states that the electric field of emitter A at the position of emitter B is the same as the electric field of emitter B at the position of emitter A, if the emitters are identical. In this case, the

numerical simulation requires only one unit cell with periodic boundary conditions. By sending in a plane wave at incidence angle θ and azimuthal angle ϕ , the electric field at position \mathbf{r} will then correspond to the far-field electric field in the direction (θ, ϕ) created by an emitter at position \mathbf{r} .

When one is interested in the normally-directed intensity (as in Publication IV), it suffices to send in normal-incidence plane waves at two orthogonal polarizations.

3.2.2 Purcell factor

The definition of the Purcell factor, $\mathcal{P} = \gamma_{\text{tot}}/\gamma_{\text{tot},0}$, can be written in terms of optical power by multiplying both emission rates by $\hbar\omega$, the photon energy. The Purcell factor is then defined as $\mathcal{P} = P_{\text{tot}}/P_{\text{tot},0}$, where P_{tot} is the total power flowing out of the oscillating dipole and $P_{\text{tot},0}$ is the power emitted by the same dipole in a homogeneous medium. The latter is given by

$$P_{\text{tot},0} = \frac{|\mathbf{p}|^2 k^4}{12\pi\epsilon^2\eta}, \quad (3.5)$$

where \mathbf{p} is the dipole moment, and the wavenumber k , permittivity ϵ and impedance η are those in the homogeneous medium. The total power P_{tot} can be calculated in two ways. First, one can directly find it by, e.g., integrating the Poynting vector over a small sphere that encloses the dipole. Second, one can determine the electric field backscattered by the structure and calculate the power from that [47, 52], by using the equation

$$P_{\text{tot}} = P_{\text{tot},0} + \frac{1}{2}\text{Re}\{\mathbf{j}^* \cdot \mathbf{E}_{\text{back}}\}, \quad (3.6)$$

where $\mathbf{j} = -i\omega\mathbf{p}$ is the dipole's electric-current amplitude and \mathbf{E}_{back} is the backscattered field (the effect of the dipole's self-field is included in $P_{\text{tot},0}$). Such calculations may be performed analytically by using a transfer-matrix method in layered media, by using the electric-current decomposition method of Publication II in homogenizable metamaterials, or by full-wave numerical calculations in the presence of any nanostructure.

3.2.3 Pump enhancement

As long as the pump light can be approximated as a plane wave incident onto the structure, the pump enhancement factor can be determined by calculating the intensity enhancement for the plane wave, which is a straightforward calculation with only one unit cell required in the computational domain. As stated previously, the pump enhancement factor is $F_p = I_p/I_{p,0}$, where I_p is the intensity of the plane wave at a point inside the structure, and $I_{p,0}$ is the intensity of the same plane wave in a homogeneous medium (the reference case). In this work, it is assumed that the emitters are insensitive to the local polarization of the pump light.

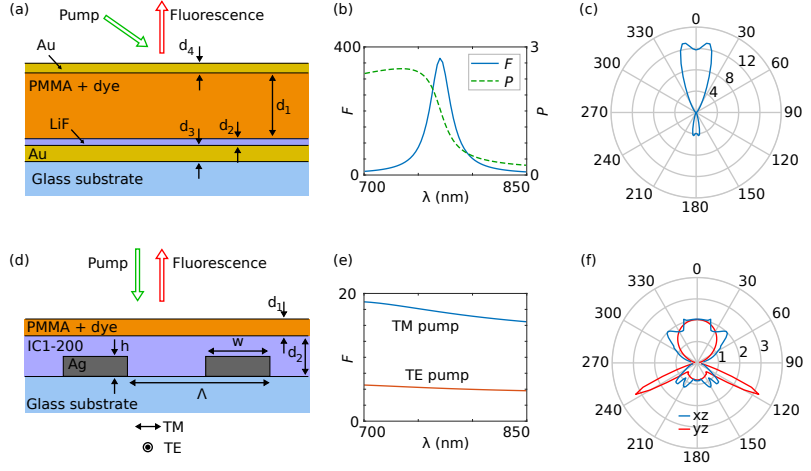


Figure 3.1. Planar microcavity resonator: (a) Structure. (b) Spectra of fluorescence enhancement factor F (blue curve) and Purcell factor P (green curve). (c) Radiation pattern at 770 nm. Grating metasurface: (d) Structure. (e) Spectra of fluorescence enhancement factor F for TM- and TE-polarized pumping (blue and red curves, respectively). (f) Radiation pattern at 770 nm.

3.3 Experimental demonstration

One of the key claims of Publication IV is that by optimizing both the emission and pump enhancement factors in the whole structure, the *average* fluorescence enhancement factor can be made very large. We demonstrated this experimentally with a planar Fabry-Perot microresonator. Figure 3.1(a) shows its structure, comprising a thick gold film acting as the bottom mirror, a thin gold film acting as the top mirror, and in between of them the fluorescent medium which is a poly(methyl methacrylate) film doped with IR-780 organic dye. There is additionally a very thin layer of lithium fluoride on top of the bottom mirror to prevent contact between metal and the dye molecules. As is well known, a Fabry-Perot resonator with highly reflective mirrors provides field enhancement in the cavity between the mirrors. An emitter inside the resonator therefore couples well to the resonant cavity modes, making its emission pattern more directional as well as changing its spectrum [59, 72–76]. The field enhancement also permits the enhancement of pump absorption. Both pump absorption and emission directivity improvements can be obtained simultaneously, as in this example.

The structure is designed such that at the fluorescence wavelength of 780 nm the structure is resonant for normally-directed waves. The emission is thereby concentrated in the normal direction. Furthermore, we designed the structure to enhance the pumping as well at a 650 nm wavelength. At this wavelength the Fabry-Perot resonance appears when the pump wave

is incident at a 57° angle. In calculations [see Fig. 3.1(b)] we predicted a fluorescence enhancement factor of 350, which arises from a combination of emission directivity enhancement and pump enhancement. The Purcell factor is modified only little: unlike three-dimensional resonators, this resonator only confines light in one dimension and so does not attain a similar mode volume reduction. The directivity enhancement is seen directly in Fig. 3.1(c), which shows the radiation pattern of the emitters in the structure, averaged over all dipole orientations. This is azimuthally symmetric, so it corresponds to a cone with a full width at half maximum of 40° .

To show that the enhancement can also be made polarization-sensitive, we designed a sample based on a grating [see Fig. 3.1(d)]. The silver stripes of the grating are embedded in glass (the glass substrate below, and spin-on-glass IC1-200 above), with the fluorescent PMMA film on top of the spin-on-glass layer. The grating exhibits a surface lattice resonance when the period matches the wavelength. We use this effect to enhance the pump wave intensity, which contributes most of the enhancement factor of about 18 seen in Fig. 3.1(e) for a TM-polarized pump wave (with electric field perpendicular to the grating stripes). For a TE-polarized pump wave the enhancement factor is only about 5 as the interaction is not as resonant. In this case the enhancement is largely independent of the fluorescence wavelength, unlike in the case of the Fabry-Perot resonator that has a narrow-band resonance. The radiation pattern of the grating structure [Fig. 3.1(f)] is quite wide, but with most of the energy directed towards the top side of the structure [red arrow in Fig. 3.1(d)] as the grating acts as a mirror for the fluorescence wavelength that is longer than the grating period. Spikes in the radiation pattern appear at 60° angles in the yz -plane of the structure, due to the excitation of surface plasmons on the grating stripes.

In addition to the resonator samples, I made samples that lacked the top Au film, as well as ones with just the PMMA film on glass. These served as reference samples. The fabrication procedure of the samples is described in more detail in Publication IV. Briefly, I deposited metal and LiF films by electron-beam evaporation and resistive thermal evaporation, respectively. Titanium was used as an adhesion layer between glass and Au to attain smooth films; no adhesion layer was required between gold and PMMA. I made PMMA films by spincoating; for this, toluene was used as a solvent for PMMA and the IR-780 dye (dissolved in methanol) was added to the mixture. PMMA films spincoated from a toluene solution tend to be thinner and more uniform than when anisole or chloroform is used as the solvent [77]. The grating structure was fabricated by electron-beam lithography.

For the optical measurements, we built a fluorescence microscope. As the goal was to measure the intensity enhancement in the far field, we chose

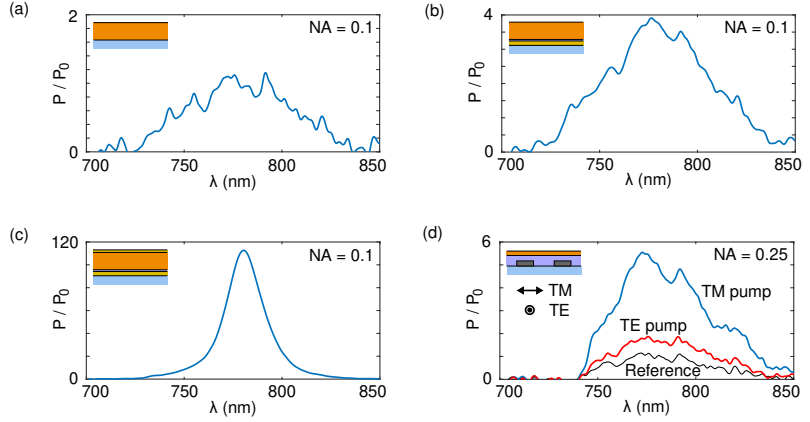


Figure 3.2. Measured fluorescence enhancement spectra. (a) Fluorescent film on glass. (b) Fluorescent film on Au mirror on glass. (c) Planar microresonator. (d) Grating metasurface.

to use a microscope objective with a small numerical aperture (0.1). This collects light emitted in the normal direction in a cone with 6° half width. The captured light is directed onto an achromatic lens that couples it into a multimode fiber that is connected to a fiber-coupled spectrometer. We used a 650 nm laser beam as the pump, focusing it to a $100\ \mu\text{m}$ spot from the side with a separate lens. Though the pump is not on the main optical axis, scattered pump light is still captured by the objective, and so this part of the spectrum was blocked with a longpass filter.

Figure 3.2 shows the experimentally measured fluorescence enhancement spectra. The reference sample is just a fluorescent film on glass [Figs. 3.2(a)]; all other “raw” spectra are divided by the *peak value* of this reference spectrum. I note here that one would normally wish to divide the spectra wavelength-by-wavelength, such that the shape of the fluorescence spectrum of the emitters would not affect the result. This makes the spectrum very noisy, however, given the modest signal-to-noise ratio of the measurement. With that said, to us the peak value is of main interest. For the planar microresonator we obtain a fluorescence enhancement factor of 120 [Fig. 3.2(c)]. For the grating we get a factor of 6 for TM and 2 for TE polarized pump light [Fig. 3.2(d)]. The measured enhancement factors are considerably lower than the predicted factors. We analyze this in more detail in Publication IV, but for resonant structures such as these, small fabrication imperfections can lead to large decreases in the performance and these are likely to blame for the difference.

The fluorescence enhancement factors obtained here can be compared to those achieved in previous work. Simply comparing numbers to numbers, even the experimental factor of 120 that we obtained from the planar microresonator exceeds the factors obtained from more complex

structures [15, 36–38, 78, 79]. This hints that the approach of optimizing the pump and emission enhancements together is fruitful. The volume-averaged fluorescence enhancement factor we used here is a relevant figure of merit in applications where the idea is to enhance the intensity of the fluorescence in the far field, that is, the brightness. Clearly this is useful in light sources, but also in detection. While one might be tempted to think that in fluorescence microscopy and chemical detection one can always use an objective lens with a large numerical aperture to capture a significant part of the fluorescent emission, such objectives typically also have very short working distances, which may limit how far into the sample one can see. Furthermore, there has been substantial interest in wavelength-conversion-based detection [80–82] where large-area fluorescence enhancement techniques may become very useful.

4. Metamaterial polarization manipulation: a metal-dielectric wave plate

Chapters 2 and 3 concentrated on the first element of any optical system, the *generation* of light. In this chapter, I move on to the topic of *controlling* light that has already been generated. Nanostructured materials offer many possibilities in this regard, and one of the most prominent aspects is the control over the polarization of light. Polarization describes the behaviour of the electric field vector of an optical wave, namely, its direction and possible correlations and phase delays between the different vector components. An important optical component for the analysis and control of polarization is the wave plate, which provides different phase shifts for two orthogonal polarization components of light passing through it. The difference in the phase shifts is known as *retardance*. Depending on the application, wave plates may have a constant, position-independent retardance, or the retardance may vary as a function of position (for example, a “spiral” wave plate has azimuthally-varying phase shifts for the purpose of generating optical beams that carry orbital angular momentum). Furthermore, the term “wave plate” often implies that it provides retardance between two orthogonal *linear* polarizations, but this is only a convention: wave retarders made of optically active media provide retardance between orthogonal *circular* polarizations instead.

Here and in Publication V I consider the type of wave plate that has the same retardance over its surface and provides retardance for orthogonal linear polarizations. Most such wave plates are based on birefringent media (crystals and liquid crystals), where light polarized along the optic axis of the material experiences a different refractive index than the orthogonally-polarized light. The difference in the refractive indices is usually small: for example, in quartz at $\lambda_0 = 780$ nm it is $\Delta n = 0.009$ [83, 84]. A quarter-wave plate ($\pi/2$ retardance) made of quartz would therefore have to be $20\text{ }\mu\text{m}$ thick. In practice, crystals are normally not grown in such small thicknesses and wave plates are considerably thicker, so-called *multi-order wave plates* for which the retardance is $\pi/2 + 2\pi m$ with m being an integer. These have narrow bandwidths, which is why we have *zero-order wave plates* where two quartz slabs with slightly different

thicknesses and orthogonal optic axes are used to cancel the $2\pi m$ part, resulting again in a $\pi/2$ retardance and relatively broadband operation. The other traditional method for building wave retarders is to use total internal reflection in prisms. Very broadband operation can be achieved with these devices, but they are fairly bulky [85–88].

4.1 Nanostructures and birefringence

Nanostructures can be designed to have much larger birefringence than ordinary crystals, and so they offer a possibility to construct broadband wave plates that are also very thin. For a simple example, let us consider a subwavelength dielectric grating made of rectangular grooves in a glass substrate [89]. The first polarization mode of this structure is the transverse electric one, with an electric field pointing along the grooves. The second is the transverse magnetic mode with electric field perpendicular to the grooves. The field distributions for these two are very different due to electromagnetic boundary conditions: for TE waves the electric field is continuous across the glass-air interfaces and concentrated in the glass, whereas for TM waves there is a discontinuity and the field is concentrated more in air. As such, the effective refractive indices of these modes are different and we have a highly birefringent structure (for example, $\Delta n \approx 0.2$ in Ref. [89]). Here, the birefringence does not come from microscopic material properties but from the structure, and is sometimes called *form birefringence*. Nanopillar metasurfaces work on the same principle but they are structured in all three dimensions instead of just two [90].

Dielectric nanostructures made of glass or photoresist polymers must still be fairly tall to achieve enough retardance to build, say, a quarter-wave plate. Using higher-refractive-index materials such as titanium dioxide is therefore advantageous, because the index contrast between TiO_2 and air is larger. Even better contrast is achieved with silicon [91], but using Si limits the operating wavelength to about 800 nm and above because Si is absorptive below this wavelength. With metal nanostructures one also encounters absorption loss but can achieve very high birefringence (I will describe the physical principle of this in the next section). However, previously, nanopatterned metal surfaces have been only demonstrated to act as wave plates in the reflection mode [92], while the transmission mode is usually more convenient. Plasmonic metasurfaces with resonant metal nanostructures also work and are very thin, but they are typically narrowband and rather lossy [93, 94]. Other metasurfaces designed as background-free wave plates produce the output light at an angle with respect to the input beam [95, 96].

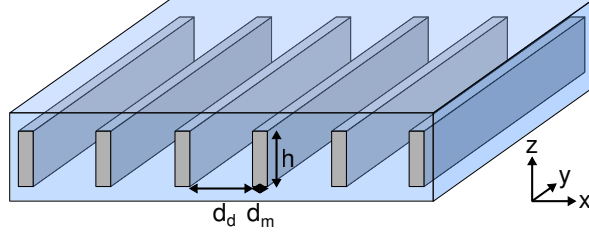


Figure 4.1. The structure of a metal-dielectric wave plate, consisting of an array of thin metal plates placed vertically in a dielectric host medium.

4.2 Design

The metal-dielectric wave plate we designed consists of alternating layers of silver and glass, as shown in Fig. 4.1. One can replace silver and glass with other metal and dielectric materials if needed, but silver provides the lowest loss of all metals at visible and near infrared wavelengths. To understand the physical reasoning behind this design, let us consider the propagation of normally-incident light through this structure. Assuming first that the metal parts are fairly thick, each of the glass “cells” can be seen as a waveguide between two metal mirrors. In such a waveguide, the TE and TM modes have radically different propagation constants because of the difference in boundary conditions. For the TE mode, the electric field is parallel to the metal stripes and, ideally, is reflected from them such that the field must be zero at the metal-dielectric interface. The electric field in the glass then has a cosine-like profile, $E = E_0 \cos(k_x x) \exp(ik_z z)$. Here, $k_x = \pi/d_d$ for the first-order mode, and therefore $k_z = \sqrt{k_0^2 n_d^2 - k_x^2}$. The propagation constant k_z is therefore smaller than the propagation constant in homogeneous glass, leading to a low effective refractive index of the mode. In contrast, for the TM mode the electric field is mostly perpendicular to the metal-dielectric interfaces and, therefore, does not need to be zero there. The electric field is then of the form $E = E_0 \exp(ik_z z)$ where $k_z = k_0 n_d$ and the effective refractive index is equal to the refractive index of the glass. One might note that if d_d becomes small enough (about $\lambda/2$), k_z will become imaginary and the TE mode will be evanescent. This is the regime where the structure turns into a wire-grid polarizer. In contrast to this, for a wave plate we keep d_d large enough.

When we consider the situation more accurately, we must account for the finite penetration depth of light in the metal. This tends to make the effective refractive indices of both the modes slightly larger: the TE mode is not so strictly confined, and the TM mode excites (non-resonant) surface plasmons on the metal-dielectric interfaces. The effective refractive indices of the modes can be determined analytically. This is simple though algebraically tedious: one writes the field in each region (metal

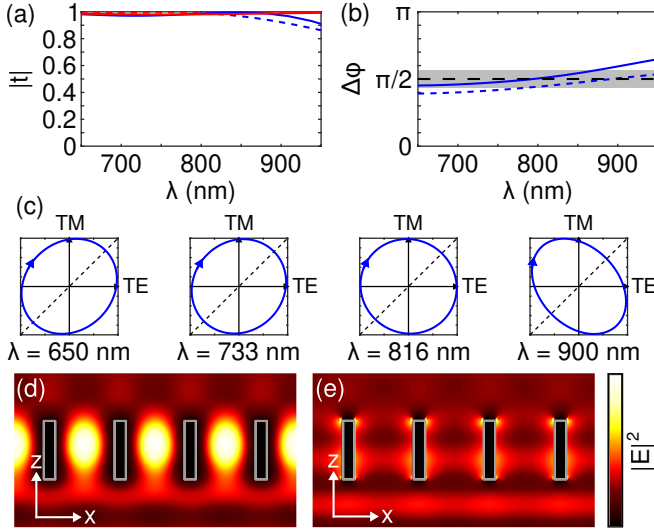


Figure 4.2. Numerical analysis of a metal-dielectric quarter-wave plate. (a) Magnitude of transmission coefficient as a function of wavelength for the TE and TM polarizations (blue and red lines, respectively). (b) Retardance, with the shaded region showing values $\pi/2 \pm 0.2$ rad. In this plot and (a), the solid and dashed lines show results obtained from full-wave and analytical calculations, respectively. (c) Polarization ellipses of transmitted waves, when the input wave is 45° linearly polarized (along the dashed line). (d) Intensity distribution of TE polarized wave at $\lambda_0 = 790$ nm. (e) Intensity distribution of TM polarized wave.

and dielectric) as a sum of two plane waves, all of which have the same k_z . The region-specific solutions are matched at the metal-dielectric interfaces by the electromagnetic boundary conditions. This results in an eigenvalue problem that, at each frequency, can be solved for k_z ; the characteristic equations to be used for this are given in Publication V. This gives the propagation constants in an infinite metal-dielectric medium. To take into account the wave plate's boundaries, we can introduce an effective impedance which turns out to be $\eta = \eta_0/n_{\text{eff}}$ for both the TE and TM modes, and use it to calculate the transmission and reflection coefficients, just as we did with metamaterials in Publication I. This is an approximation, as it relies on the assumption that the incident wave excites only the first-order mode. In reality, many higher-order-modes are excited. These do not propagate in the structure, but they change the transmission and reflection characteristics of the waveplate-glass boundaries. Also, at oblique incidence angles, some higher-order modes can be excited even if they are forbidden at normal incidence. We encountered this situation in a later work [97], and I will not elaborate on it here.

The analytical method just described facilitates fast optimization of the structure to minimize absorption and reflection losses while keeping the birefringence high. Figure 4.2 shows the calculated optical characteris-

tics of a quarter-wave plate with the design wavelength of 780 nm. The transmission is high, over 95 % in a broad wavelength range [Fig. 4.2(a)], and the retardance stays within ± 0.2 rad of the $\pi/2$ value from 650 nm to 850 nm [Fig. 4.2(b)]. This wavelength range covers a 110 THz bandwidth which is enough, for example, to cover the entire spectrum of a 10 fs optical pulse. Figure 4.2(c) shows the polarization ellipses at four equally spaced wavelengths; at 780 nm the ellipse is ideally circular, and the eccentricity at 650 nm and 900 nm is a result of deviation from the $\pi/2$ phase shift. Finally, Figs. 4.2(d) and 4.2(e) show the intensity distributions of a plane wave propagating through the structure with TE and TM polarization, respectively. As stated earlier, the TE mode has field maxima at the centers of the dielectric parts while the TM mode is slightly concentrated at the metal-dielectric interfaces. The field distributions also demonstrate that the low absorption loss is due to the fact that the intensity is concentrated in the glass, not penetrating much into the metal.

4.3 Experimental demonstration

We fabricated and characterized the wave plate described above. Recognizing that it is normally challenging to fabricate tall and thin metal nanostructures, we used a fabrication method based on oblique-angle deposition of metal films followed by plasma etching (we developed the method independently, though a similar one had been previously described in [98]). The method is outlined in Fig. 4.3. Traditional electron-beam lithography steps with PMMA resist [(a) and (b)] are used to create an array of PMMA stripes [seen in (c)]; these form the dielectric part of *every other* unit cell. A sacrificial layer of aluminium is deposited by electron-beam evaporation, which will be etched later. Silver is then deposited by e-beam evaporation at two opposite angles, such that a silver film is grown on the sidewalls of the PMMA stripes and on the top while the bottom surface is shadowed. Reactive ion etching with argon is then performed (at normal incidence) to remove the top silver layer, and followed up with chemical etching of Al to remove any remaining silver that inevitably gets re-deposited during plasma etching. To finish the structure we spincoat a layer of PMMA, filling the gaps and covering the structure. The scanning electron microscope images showcase the fabrication quality: This method is eminently suitable for fabricating tall, narrow, large-aspect-ratio structures. Furthermore, for structures with one-dimensional periodicity, the electron-beam exposure step could be replaced with an optical interference lithography [99] or nanoimprint lithography step [100]. Both of these methods are suitable for fast fabrication of large-area structures. This also makes our waveplate design suitable for mass production.

For the optical measurements we used a home-built microscope with

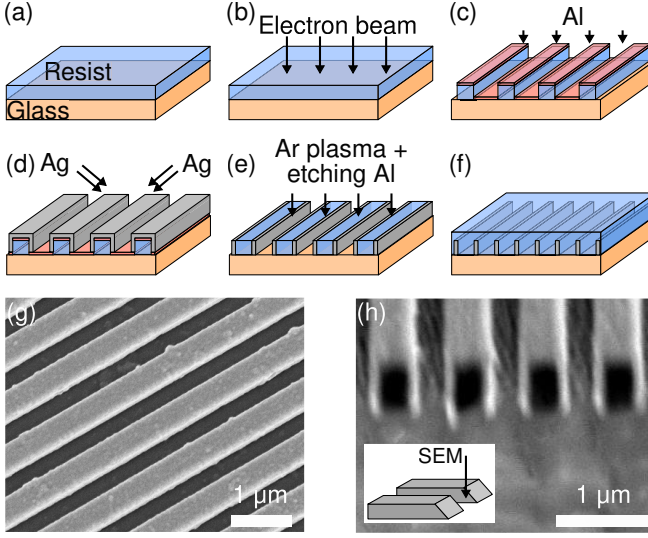


Figure 4.3. Fabrication of the wave plate. (a) Spin-coating of PMMA resist. (b) Electron beam exposure. (c) Deposition of Al sacrificial layer. (d) Deposition of Ag at oblique incidence. (e) Ar plasma etching followed by chemical Al etching. (f) Spin-coating of PMMA. (g) Scanning electron microscope image taken after step (d). (h) SEM image of a ion-beam-milled cross section of the sample.

one microscope objective (numerical aperture 0.1) focusing the light of a fiber-coupled xenon lamp onto the sample and another objective collecting the transmitted light, which then was sent to a fiber-coupled spectrometer. We used a polarizer before the sample to set the 45° linear polarization state, and then an analyzer after the sample, to measure the transmitted spectra at the 0° , 30° and 90° linear polarizations. The transmittances t_x and t_y are obviously computed from the 0° and 90° measurements, while the retardance can be computed from the 30° measurement through

$$\phi = \arccos \left\{ \frac{t_x \cos(\theta)^2 + t_y \sin(\theta)^2 - t_{30}}{2 \cos \theta \sin \theta t_x t_y} \right\} \quad (4.1)$$

where $\theta = 30^\circ$ in this case. This equation is easily proved using the Jones matrix formalism [32].

The measured optical properties of the wave plate are shown in Fig. 4.4. Comparing them to the numerically predicted properties in Fig. 4.2, we see that the transmission is slightly lower, while the retardance is more or less as predicted. The transmission losses are connected to fabrication-related imperfections, chiefly reflection from any remaining metal at the bottom and top surfaces of the PMMA grating.

For a scientist, this wave plate is interesting because it challenges the conventional notion that metallic structures operating in transmission mode are usually quite lossy. The “trick” of the design is that the electric field of the incoming wave is not allowed to penetrate the metal, by leaving

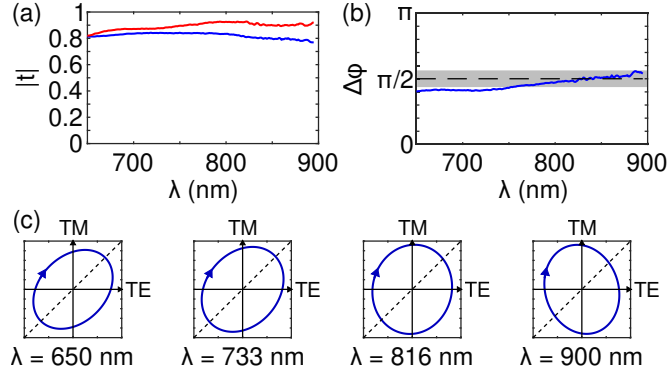


Figure 4.4. Experimental characterization of a metal-dielectric waveplate. (a) Magnitude of the transmission coefficient as a function of wavelength for the TE and TM polarizations (blue and red lines, respectively). (b) Retardance, with the shaded region showing values $\pi/2 \pm 0.2$ rad. (c) Polarization ellipses of transmitted waves, when the input wave is 45° linearly polarized (along the dashed line).

enough room for the field to exist mostly in the dielectric parts. The plasmonic resonance frequencies of the structure are also nowhere near the operating frequency. For an engineer, a key advantage of this structure over other thin wave plates is that, as a one-dimensional grating, it can be easily fabricated on a large scale, is broadband, and the design can be adapted for many wavelength regions. It would also be very interesting to study how far the bandwidth of this wave plate design can be extended by utilizing one of the multi-wave plate bandwidth extension methods [86–88].

5. Sub-picosecond all-optical modulation and detection

The last topic of this dissertation is ultrafast all-optical modulation and detection, moving from *linear* control of light as in the previous chapter to *nonlinear* control. In Chapter 1 I outlined the importance of all-optical modulation to optical information processing systems and optical computers. I also mentioned the main problem that persists in this area: nonlinear optical effects required for all-optical modulation tend to be either fast and weak or slow and strong. To improve performance without requiring too much power, a fast and strong optical nonlinearity is required.

Although no nanostructures will be discussed here, the topic has a very immediate connection to nanophotonics for two reasons: first, nanophotonics-based approaches are often used to enhance the light-matter interactions discussed here, and second, modulators and detectors are most commonly used in integrated and fiber optics, in which nanophotonics makes contributions.

5.1 Optical nonlinearity at sub-picosecond time scales

The fastest phenomena that could conceivably be used for optical modulation are the optical Kerr effect and two-photon absorption, third-order nonlinear effects with few-femtosecond response times brought about by the deformation of the electronic energy states of molecules [29]. The Kerr effect provides phase modulation due to an essentially instantaneous change in the refractive index, and two-photon absorption provides amplitude modulation due to a change in the absorption coefficient (in semiconductors it also results in nonlinearities related to carrier excitation [101]). These two are interlinked: materials with high nonlinear refractive indices (a measure of the strength of the Kerr effect) usually have elevated two-photon absorption coefficients as well [30]. This connection is due to the causality constraint described by the Kramers-Krönig relations. Still, these effects are weak: for a back-of-the-envelope calculation example, consider hydrogenated amorphous silicon, one of the premier nonlinear

materials at near-infrared wavelengths, with a nonlinear refractive index $n_2 = 4.2 \times 10^{-17} \text{ m}^2/\text{W}$ [102]. If light is coupled into a waveguide with $1 \mu\text{m}^2$ mode area and 1 cm length, an instantaneous power of about 2 W must be coupled into the waveguide to cause a π phase shift for a signal propagating in the same waveguide. Shorter waveguides, required in high-density optical chips, would require correspondingly higher power. In all-optical switching, the instantaneous power together with the bit time determine the switching energy. In the example above, should the bits be 100 fs, long the switching energy would need to be approximately 200 fJ, which is unfortunately large compared to what is achieved in modern nanoelectronics (where 0.1 – 10 fJ switching energies are obtained, albeit at much lower speeds [103]).

Stronger but still fast nonlinearities include intraband pumping in semiconductors, where the charge carriers of a partially-filled electronic band are excited to higher energy levels within the same band, from where they then decay quickly back to the original levels [104]. The relaxation time in this process is on the order of 100 fs. Here the carriers at excited energy levels have a different optical response when compared to the original levels. Similarly, pumping a gain medium changes the populations of its energy levels, which manifests itself in a change in the optical response. The onset of change can be fast (on the order of 10 – 100 fs), but the population change relaxes in a nanosecond time frame, which is far too slow to be called ultrafast [31, 32, 105, 106].

To try and solve the conundrum of not having a simultaneously fast and strong nonlinearity, there are a number of approaches. To strengthen any type of nonlinearity, one can use a resonator or a waveguide to provide field confinement and enhancement [21, 22, 33–35]. This way, significant phase and amplitude modulation have been demonstrated with switching energies as low as 0.4 fJ in a photonic crystal cavity [21], no more than a few thousand photons. However, resonators introduce a tradeoff between the bandwidth and field enhancement. As outlined in Chapter 1, a high Q -factor resonator provides high field enhancement but limits the bandwidth (in the photonic crystal cavity mentioned above, the $Q = 2500$ resonator was capable of 20 ps switching, that is, a 50 GHz rate). For nonlinearities that switch on rapidly but relax slowly, the overall speed can be augmented with differential switching schemes [107] and turbo switching [108], which compensate for the slow parts of a nonlinear response. The ultimate limit of these techniques is, however, unclear (640 GHz modulation in semiconductor optical amplifiers has been discussed [109]). In the next section I propose a method to use a slowly relaxing gain medium to perform all-optical modulation, pushing the modulation speed to the sub-picosecond regime by spectral addressing.

The limitations of speed apply to detection as well as modulation. I discuss the ways to overcome these limits in Sec. 5.3.

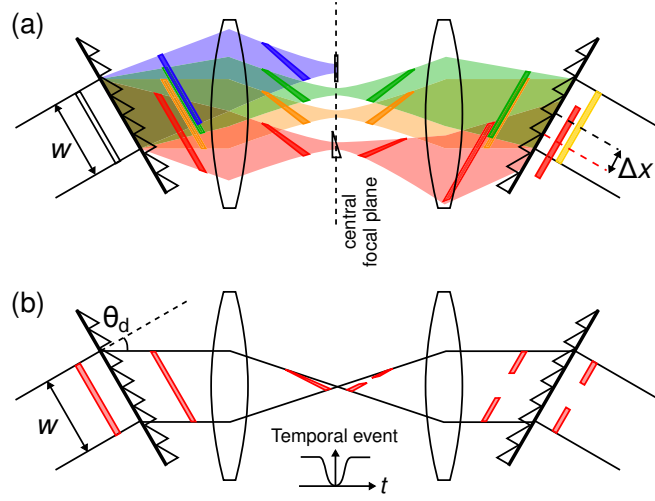


Figure 5.1. Fourier transform pulse shaper schematic. (a) Wavelength splitting function. (b) Space-to-time mapping function.

5.2 Spectrally-addressed all-optical modulation

The key to sub-picosecond all-optical modulation without requiring sub-picosecond response from the underlying nonlinear effect is to divide the signal into its wavelength components, modulate each, and then recombine them. As each wavelength component varies much more slowly than the full optical waveform, they can be modulated with slow-response nonlinear effects, and yet obtain a fast modulation at the end. This can be understood in two ways: as an optically-addressed pulse shaper, or as a wavelength division multiplexing-based modulator.

In this work the device that performs the wavelength splitting and recombining is a Fourier transform pulse shaper [110], a well-known optical system depicted in Fig. 5.1. In this bulk-optics form it consists of a grating that maps wavelength to propagation angle, a lens that maps the propagation angle to spatial position, and another lens and grating to undo this operation by recombining the waves. At the central focal plane of the device, one inserts a transparency that changes the phase or amplitude of each of the wavelength components. Each wavelength is mapped to a transverse position according to

$$x = \frac{(\lambda - \lambda_c)L}{\Lambda \cos(\theta_d)}, \quad (5.1)$$

where λ_c is the central wavelength, L is the focal length of the lenses used in the system, and θ_d is the diffraction angle. As the name suggests this device has been traditionally utilized for shaping pulses from mode-

locked lasers for purposes such as chirp control, pulse train generation and quantum system control [111]. Often the transparency is provided by a spatial light modulator, which makes the pulse shaper reprogrammable.

Our idea is to insert a gain medium in the central focal plane and pump it with an optical beam, making the device act as an optically-addressed pulse shaper. The pump beam modulates those spectral components that it overlaps with. Furthermore, even if the signal input is a short pulse, the temporal pulse width at the central focal plane is determined by the pulse shaper and is given by

$$T = \frac{w \sin(\theta_d)}{c \cos(\theta_d)}, \quad (5.2)$$

where w is spatial width of the input beam. Two equivalent pictures explain this. First, the first grating gives the input pulse a spatio-temporal tilt as shown in Fig. 5.1(b). Clearly, when the pulse is focused, the tilt translates into a longer pulse. Second, the dispersion of the wavelengths at the central focal plane makes the *local* spectrum much narrower, which by virtue of the Fourier transform, corresponds to a longer pulse in time. For all-optical modulation, this increased pulse width allows us to utilize the strong but slowly recovering optical pumping of a gain medium as the underlying modulation mechanism.

Modulation in this system is most convenient if we operate it as a pulse-by-pulse shaper, not actually generating new frequencies but using the pump beam to generate a new “spectral filter” for each of the input signal pulses. Two modulation rates are relevant in this system: the overall rate (modulation rate over multiple pulses, equal to the symbol rate of the system if used in a multiplexing capacity) and the instantaneous rate. Assuming the signal beam is a train of mode-locked pulses with repetition rate f_{rep} and spectral width Δf , the overall modulation rate is obviously limited to Δf ; this is the Nyquist limit. In practice this would require addressing each of the frequency comb lines independently, requiring a spectral resolution of $\Delta\lambda = \lambda^2/(cf_{\text{rep}})$. In fact, the spectral resolution of the pulse shaper is

$$\Delta\lambda = \frac{\Lambda \cos(\theta_d)}{w} \lambda_c, \quad (5.3)$$

and assuming this is less than the frequency comb resolution limit, the overall modulation rate will be

$$\Delta f_{\text{overall}} = f_{\text{rep}} \frac{\Delta\lambda_{\text{tot}}}{\Delta\lambda}, \quad (5.4)$$

where $\Delta\lambda_{\text{tot}}$ is the total spectral width of the probe beam. Turning to the instantaneous modulation rate, it is limited only by the probe’s spectral width, $\Delta f_{\text{inst}} = \Delta f$, simply because we can quite arbitrarily control the whole spectrum, creating signals with that bandwidth.

How the pump beam is sent into the system depends on the task at hand. In the experiments described later, we used a pump beam that

bypassed the first grating. The spatial distribution of this beam needs to be controlled to address different spectral components of the signal beam. It is also possible to send the pump beam through the grating, in which its spatial distribution at the central focal plane is determined by its spectrum. This is obviously much better from the point of view that if the pump spectrum is changed it immediately translates into the modulation. In the bypass configuration the beam would have to be scanned or spatially modulated to quickly change the modulation pattern.

5.3 Ultrafast signal detection

Equally important as the creation of ultrafast waveforms is their detection. This takes place not only in communication systems where broadband optical signals are converted into electrical signals, but also when ultrafast phenomena such as chemical reactions are studied using optics [112, 113]. As mentioned in the introduction, the fastest semiconductor photodetectors have bandwidths on the order of 100 GHz, allowing a time resolution of 10 ps. To resolve sub-picosecond waveforms, a number of techniques have been developed and they vary widely in their capabilities. One particular dividing line is between active and passive methods [113]. In an active method, a prepared type of illumination is used to probe an event and the optical signal due to the event is imprinted onto the light. In a passive method, no special illumination is used and the signal can come from any source. Another important consideration is that single-shot techniques can retrieve the whole signal by measuring, e.g., a single laser pulse, whereas other techniques need an event that repeats many times to obtain a signal.

The most straightforward solution aside from direct photodetectors are streak cameras [114] that use a vacuum tube with a photosensitive surface where the optical intensity is transduced into an electron beam, and then voltage-swept electrodes redirect the photoelectrons into different directions based on their time of generation. This allows an array detector to capture the optical intensity variation as a spatial trace. Many optical techniques also utilize the principle of mapping time to space. This was perhaps first used in single-shot pump-probe measurement techniques [115, 116], in which short pulses travelling at an angle with respect to each other have a time delay that depends on the spatial position. Another technique is to use an echelon grating or beam splitters and delay lines to create a burst of ultrashort pulses. They are then either sent to a sample at slightly different incidence angles, which again places them at different positions on an array detector [117], or they can be separated through holographic methods [118]. Such a technique can capture two-dimensional images, acting as an ultrafast equivalent of a video camera. The pulse splitting can also be done by applying chirp on the pulse and then using spectral

filters to select different times (STAMP [119] and SF-STAMP [120]). A multitude of other mapping-type techniques exists [113]. Especially when spatial information is obtained together with temporal information, the techniques mentioned here are often called *temporal imaging*.

For the detection of one-dimensional (time only) signals, there are techniques that work on a different basis. Time lenses utilize quadratic phase modulation to temporally “magnify” a signal, allowing direct photodetection [121] (this technique *also* bears the name “temporal imaging” due to its analogy to spatial image formation by lenses). Cross-phase modulation with chirped ultrashort pulses can be used to achieve a sub-picosecond resolution. One could also mention the traditional pulse-shape-measurement techniques in ultrafast optics, such as autocorrelation, frequency-resolved optical gating and variants thereof [31], but these almost always require a relatively long time for measurements and a repeating signal due to the scanning delays and weak signals. Traditional pump-probe spectroscopy, utilizing a varying optical delay between an exciting and a sensing pulse, also falls in this category. Most of the techniques discussed here obtain the signal information directly in the time domain. Technically, however, we may consider the demultiplexing operation in frequency-comb-based wavelength division multiplexing (where the spectral channels are coherent with respect to each other) to be a form of ultrafast detection as well, because if both the phase and amplitude of each channel are measured, then the time-domain signal can be reconstructed by inverse Fourier transformation.

Here, we developed an active technique for ultrafast signal detection that utilizes spatio-temporally tilted laser pulses seen in a Fourier transform pulse shaper [refer back to Fig. 5.1(b)]. It is based on realizing that once the tilted pulse is focused, the leading part (on the right side when looking in the propagation direction) will pass through the focal point first and then the rest of the pulse later. This way, space (the transverse coordinate before and after the lenses) is mapped into time (at the central focal plane). If a short temporal event causes, say, a dip in the transmittance of the sample, then there will be a corresponding dip in the temporal profile of the pulse. This is also reflected in the transverse intensity distribution. The pulse can now be collimated again by the second lens, and then its transverse intensity distribution measured to find the time behaviour of the sample at the focal region. This measurement can be done with a slow array detector.

The signal obtained by this method is

$$I(x) = |A(x)|^2 \int |S(t)|^2 |m(t - \gamma x)|^2 dt, \quad (5.5)$$

where $|A(x)|^2$ and $|S(t)|^2$ are the transverse intensity distribution and the temporal intensity distribution of the probe pulse, respectively, $|m(t - \gamma x)|^2$ is the temporal intensity modulation at the central focal plane, and $\gamma =$

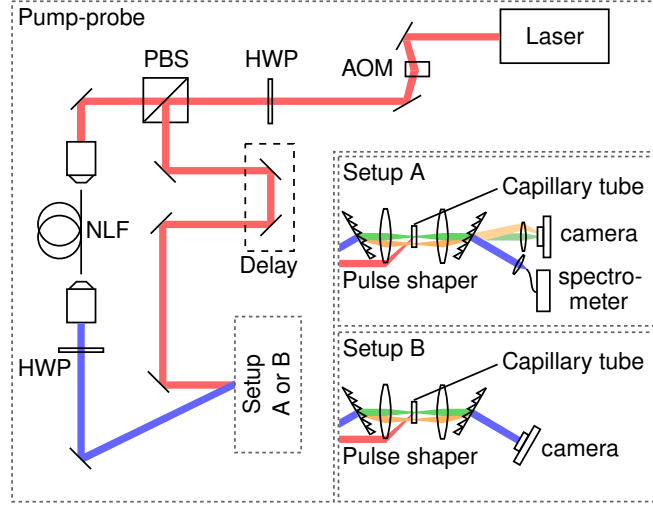


Figure 5.2. Experimental setup used for demonstrating ultrafast all-optical modulation and ultrafast detection.

$\lambda_c/(c\Lambda \cos \theta_d)$ is a space-to-time mapping factor (see Publication VI for derivations). Equation (5.5) is the cross-correlation of the signal pulse with the temporal modulation, and as such the input pulse's temporal intensity distribution acts as a kind of point-spread function. Hence, the time resolution of this technique is limited only by the width of the input pulse, so sub-picosecond resolution is easily achieved. The sequence length (time window captured by one pulse) is determined by Eq. (5.2) and chiefly constrained by the device's geometry; in devices of modest size ($w = 1$ cm), and $\theta_d = 45^\circ$ it is on the order of 30 ps. Imaging in time and one space dimension is possible with this technique, thanks to the “unused” vertical spatial dimension, but it is not demonstrated here.

5.4 Experiments

To demonstrate the all-optical modulation and detection techniques outlined above, we constructed a white-light pump-probe setup, detailed in Fig. 5.2. For clarity, I discuss it in two parts: the pump-probe part and an experiment-dependent part including the pulse shaper and detectors. In the pump-probe part, the ultrashort pulses from a fs laser are split by a polarizing beam splitter (PBS). One half, the pump pulse, goes through a delay line that allows us to control the delay between the pump and probe. The other half, the probe pulse, is first coupled into a microstructured nonlinear optical fiber (NLF) where various nonlinear processes broaden its spectrum, achieving supercontinuum generation (spanning wavelengths

from 500 nm to 1000 nm and beyond) if the input power is high enough. Most importantly, a broadband pump-probe setup like this can be used to measure transient absorption spectra. These are transmission spectra of a sample, illuminated by the spectrally-broadened probe pulse and measured with and without a pump pulse present. By varying the pump-probe delay, the appearance and disappearance of various transmission-modifying effects can be tracked as a function of both time and wavelength.

In all-optical modulation the pump pulse acts as the modulator and the probe pulse acts as the signal, whereas in detection the pump pulse acts as the source of the temporal variation of the sample and the probe pulse is the pulse used to measure the signal. The probe pulse enters the pulse shaper through the center of the grating and lens, while the pump pulse bypasses the grating and goes through the lens close to its edge; by controlling the pump beam's input angle we control the location where it is focused and thus the wavelength component that it affects. As the sample we used a 100 μm -thick capillary flow cell filled with a dye solution (IR-780 dissolved in methanol). IR-780 was selected for this experiment because of the good overlap of its absorption and emission spectra with the Ti:Sapphire laser's spectrum.

5.4.1 All-optical modulation

To demonstrate spectrally-addressed all-optical modulation we measured the transient spectra of the signal pulse in two cases. The experiment here corresponds to setup A in Fig. 5.2. In the first case, the pump beam was directed to overlap the wavelength 775 nm, which causes depletion of the ground state population and increases the probe transmission. In the second case, the overlap was at the wavelength 830 nm, where stimulated emission amplifies the probe instead. With this setup we achieved a spectral resolution of $\Delta\lambda = 0.85$ nm, probe pulse width at central focal plane of $T = 2.3$ ps, and pump pulse width of 500 fs with fluence on the order of 2.5 mJ/cm^2 which is enough to pump about one half of the molecules to the excited state. Figure 5.3(a) shows the transient spectra in the first case. The peak at 775 nm shows that the probe transmission increases but only at this wavelength, as desired. Figure 5.3(b) follows the peak value at a range of delays, where we see the modulation switch on as the pump pulse arrives. Though the pump pulse is only 500 fs long the trace here takes about 2 ps to increase, due to the probe pulse's increased width. Figures 5.3(c) and 5.3(d) demonstrate the same effect at 830 nm using stimulated emission. Finally, 5.3(e) shows the modulation in time domain, calculated by assuming that the probe is a chirped Gaussian pulse, with its spectrum amplitude-modulated as shown in Fig. 5.3(a). The blue curve is the original pulse and the red is the modulated one, in which the 250 fs oscillation shows that we indeed obtain sub-picosecond temporal

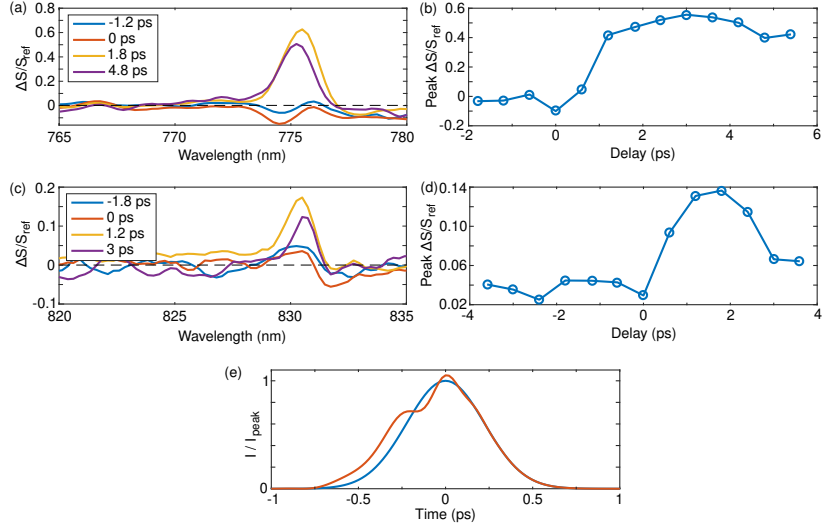


Figure 5.3. (a) Transient spectra at selected pump-probe delays when the pump is centered on the wavelength 775 nm. (b) The peak value at 775 nm as a function of the delay. (c) Transient spectra when the pump is centered on the wavelength 830 nm. (d) The peak value at 830 nm as a function of the delay. (e) Calculated temporal modulation of the signal pulse. Here blue and red curves show the pulse before and after modulation, respectively.

modulation.

The spectral width affected by the pump is 1.8 nm, which is close to the predicted spectral resolution of the pulse shaper. In this setup the spectral width of the signal pulse varies from about 10 nm to 100 nm or more (with supercontinuum generation), which means that from 6 to 60 spectral channels can be separately addressed. I point out that this is far from any practical limit. The beams are only about 3 mm in diameter and increasing the size is the most straightforward way of increasing the resolution, aside from switching to gratings with smaller period. This would also increase the effective numerical aperture, allowing tighter focusing of both the pump and probe and thus lower power to be used. In the present experiment the switching energy is set by the pump pulse energy to about 1 nJ. Were the beams focused to diffraction limit ($\lambda/2$ spot diameter for the pump) this would be 10 pJ. Further improvement would require using a gain medium with a larger absorption cross section.

To approach the ultimate limits of this technique, it would be fruitful to consider an integrated-optics-based implementation where the gratings are replaced with arrayed waveguide gratings (the integrated pulse shaper has been discussed previously [122, 123]). This would be a more robust system (not possible to misalign) and would allow for a large number of wavelength channels in a smaller device footprint.

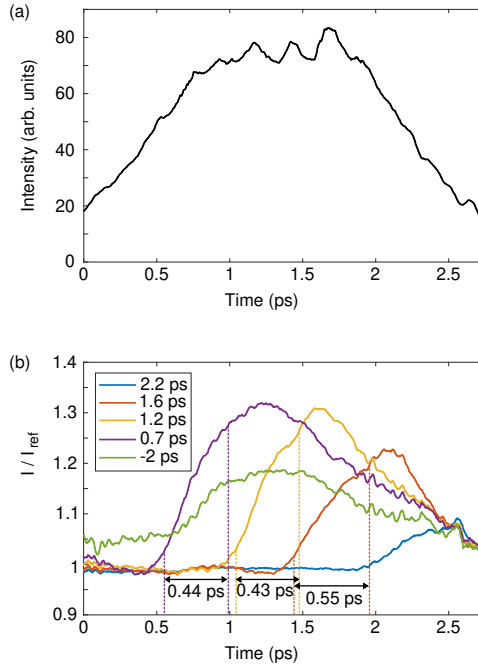


Figure 5.4. (a) Intensity distribution of the probe beam at the output of the second grating of the pulse shaper. (b) Temporal images of the transmittance of a gain medium pumped by a pump pulse at several different times, shown by different colours in the plot. The labelled intervals show the time corresponding to the full width at half maximum of the pump pulse, assuming it is Gaussian.

5.4.2 Ultrafast signal detection

To demonstrate signal detection by spatio-temporally tilted pulses, we set out to measure the gain medium's transient absorption change as the pump pulse excites the dye molecules. This was previously observed by using the delay-scanning pump-probe method [see Fig. 5.3(b)]. However, here we will obtain a single-shot temporal measurement with better resolution. For this experiment the probe pulse's spectral broadening is minimized to achieve as good spatial overlap as possible between the probe and pump pulses. As shown in setup B in Fig. 5.2, the camera is now placed right after the second grating. Technically it should be placed exactly where the grating is as this is where all the wavelength components are combined [as shown in Fig. 5.1(a)]. Here, the angular dispersion of the components is not so large and so placing it a short distance away (yet in the zeroth diffraction order) is enough.

Figure 5.4(a) shows the intensity distribution of the probe beam at the camera (pixels in the vertical dimension are averaged over to improve the signal-to-noise ratio), showing the background temporal illumination.

Switching on the pump, we obtain the transmittance of the gain medium as a function of time at a few different pump-probe delays. Figure 5.4(b) shows these by different colours. In each case the intensity increases sharply when the pump pulse arrives. In this experiment the input pulse width is 330 fs which also sets the time resolution to the same value. Ideally these curves would look like smoothed step functions (constant intensity after the jump, same amplitude for all curves), but here they vary as a function of time. We believe that lensing-induced intensity distribution changes due to population inversion-induced phase shift are responsible for this. It is worth noting that by taking the derivative of the curves in Fig. 5.4(b), one obtains the pump pulse shape (cross-correlated with the probe pulse shape as in Eq. (5.5)). Therefore, if we can assume that the initial response of the gain medium is very fast, this technique can be used to detect, e.g., amplitude modulation in the pump pulse.

A key advantage of this detection approach is its simplicity: in addition to the mode-locked laser, only a pulse shaper is technically needed. The pump-probe part in this setup facilitates easily synchronized excitation of the sample, but in general the temporal event being imaged could be initiated by a different laser or event. All probe beam power is also used in forming the temporal image, which can provide excellent signal-to-noise ratio if fluctuations are minimized. True single-pulse imaging is also possible with modest pulse energies, which is advantageous in studying samples that are photobleached or otherwise irreversibly changed upon exposure, as well as events that do not repeat exactly such as material breakdown phenomena.

Finally, I note that it is possible to use a fundamentally one-dimensional imaging device as a two-dimensional imager by utilizing compressive sensing techniques (as in compressed ultrafast photography [114]). This may be a worthwhile avenue of investigation if the technique is to be used for imaging in two spatial dimensions in addition to the time dimension.

6. Conclusions and outlook

The main focus of this dissertation has been the design and use of nanomaterials to control the generation and propagation of light, the control of spontaneous emission, and ultrafast all-optical modulation and detection. To summarize the main contributions, we developed further the theory that describes spatially dispersive nanomaterials using wave parameters, and described how optical power flows inside such nanomaterials. We then utilized the developed theory to study spontaneous emission of light in optical metamaterials. The electric-current decomposition method allows semi-analytical predictions of spontaneous emission modification in these structures, and accounts for the presence of spatial dispersion. This can yield more physical insight than just using full-wave simulations of dipole emission, and can also be much faster. Further, we studied the power flow from emitters located inside absorptive metamaterials, showing why under certain conditions light can escape such materials efficiently. Moving on to the specific case of fluorescence, we analyzed the different factors that contribute to fluorescence enhancement. Concentrating on the average fluorescence intensity from large-area nanostructures, we asserted the importance of optimizing the pump and emission enhancements together. Our experimental results demonstrated large and polarization-dependent enhancement of fluorescence intensity for structures that were designed keeping this principle in mind.

We designed, fabricated and experimentally characterized a transmissive metal-dielectric nanomaterial-based wave plate. The birefringence of the underlying nanomaterial is very strong, allowing a small thickness. The wave plate works in a broad band and has a high transmission. Though we used electron-beam lithography in the fabrication process, the wave plate could be fabricated on large areas by other processes such as interference or nanoimprint lithography.

Finally, we introduced and experimentally demonstrated a technique of all-optical modulation that achieves sub-picosecond speed while utilizing a strong light-matter interaction. Based on a pulse shaper and an on-resonance optical gain medium, the technique is simple and implementable

in integrated optics. We also introduced a new form of ultrafast detection, a temporal imaging method that uses spatio-temporally tilted laser pulses to map the temporal behaviour of a sample into a spatial distribution that can be detected by a slow array detector. This method also achieves sub-picosecond resolution.

There are many ways in which the tools for analyzing nanomaterials and spontaneous emission could be used. Taking the electric-current decomposition method, one can quickly analyze the radiation patterns of emitters inside metamaterials to a good approximation. As spatial dispersion is taken into account, the method is appropriate for realistic nanomaterials that usually have sizeable unit cells. Most designs of, for example, hyperbolic and zero-index metamaterials are like this, and these are some of the most interesting types of nanomaterials for spontaneous emission modification. These particular examples have received much attention, but there are many other intriguing types of nanomaterials as well. One example is the diffraction-compensating metamaterial studied in our work. Such a material may allow the emission from many quantum emitters to be concentrated in a beam, producing high-intensity collimated but incoherent, broadband radiation similarly to amplified spontaneous emission sources. While the fabrication of the three-dimensional metamaterials we considered here may be a daunting task at present, one could find a way to implement similar effects in a two-dimensional fashion, for example by integrating a metamaterial in a waveguide [63]. Speaking from an applications point of view, improved sensing based on fluorescence or surface-enhanced Raman scattering has been discussed as an important application of metamaterials and metasurfaces, and here, too, the analysis of spontaneous emission by our methods should prove useful.

Our design of the metal-dielectric wave plate is an example of a very concrete application of metamaterials, and one that is eminently practical because of its potential for easy fabrication and operation in the usual transmission mode with high, broadband transmission. It is also a demonstration of the fact that metal-based nanostructures can exhibit low losses (by not operating on top of a plasmonic resonance) while still exerting a strong influence on light; this is an interesting counterpoint to the “plasmonics equals high losses” picture that is often brought up when discussing nanostructures. Furthermore, wave plates of sub-micrometer thickness such as the one presented here can be of special interest in flat optics systems where space is limited.

Finally, stepping away from nanostructures and into the topic of sub-picosecond all-optical modulation and detection, what we performed here was a proof-of-principle demonstration using fluorescent molecules as the gain medium. This shows that the concept is sound, and in the future it would be interesting to perform the demonstration in a “full-scale” setup where the limits of the techniques could be experimentally explored. The

details of an integrated-optics-based implementation would also make for an interesting study, possibly answering the question whether or not these techniques could supplant or replace more traditional techniques of all-optical modulation and detection. Incidentally, I wish to note here that it is no accident that we used a dye-based gain medium in the experiments. This research project started as an exploration of the possibility of using dyes and quantum dots for all-optical modulation, utilizing the ultrafast features of their optical response. This includes the fast relaxation processes that happen after the initial excitation, which we did not yet use in the work described here. Whether or not these could be useful in all-optical modulation is still an open question. At any rate, the proposed techniques work well even with gain media with slow relaxation times. Therefore, using these techniques in conjunction with a gain medium that is impervious to photobleaching and has lower pulse energy requirements could well offer a way to make practical and powerful ultrafast modulators and detectors.

References

- [1] J. D. Joannopoulos, S. G. Johnson, J. N. Winn, and R. D. Meade. *Photonic Crystals: Molding the Flow of Light*. Princeton University Press, second edition, 2008.
- [2] D. R. Smith and J. B. Pendry. Homogenization of Metamaterials by Field Averaging (Invited Paper). *J. Opt. Soc. Am. B*, **23**, 391–403, 2006.
- [3] A. Andryieuski, S. Ha, A. A. Sukhorukov, Y. S. Kivshar, and A. V. Lavrinenko. Bloch-Mode Analysis for Retrieving Effective Parameters of Metamaterials. *Phys. Rev. B*, **86**, 035127, 2012.
- [4] P. Grahm, A. Shevchenko, and M. Kaivola. Interferometric Description of Optical Metamaterials. *New J. Phys.*, **15**, 113044, 2013.
- [5] A. D. Yoffe. Semiconductor Quantum Dots and Related Systems: Electronic, Optical, Luminescence and Related Properties of Low Dimensional Systems. *Adv. Phys.*, 2010.
- [6] R.-M. Ma and R. F. Oulton. Applications of Nanolasers. *Nature Nanotech*, **14**, 12–22, 2019.
- [7] P. R. West, J. L. Stewart, A. V. Kildishev, V. M. Shalaev, V. V. Shkunov, F. Strohendl, Y. Zakharenkov, R. K. Dodds, and R. Byren. All-Dielectric Subwavelength Metasurface Focusing Lens. *Opt. Express*, **22**, 26212, 2014.
- [8] G. Zheng, H. Mühlenbernd, M. Kenney, G. Li, T. Zentgraf, and S. Zhang. Metasurface Holograms Reaching 80% Efficiency. *Nat. Nanotechnol.*, **10**, 308–312, 2015.
- [9] J. Lu and J. Vučković. Objective-First Design of High-Efficiency, Small-Footprint Couplers between Arbitrary Nanophotonic Waveguide Modes. *Opt. Express*, **20**, 7221–7236, 2012.
- [10] B. Shen, P. Wang, R. Polson, and R. Menon. An Integrated-Nanophotonics Polarization Beamsplitter with $2.4 \times 2.4 \mu\text{m}^2$ Footprint. *Nat. Photon.*, **9**, 378–382, 2015.
- [11] V. M. Shalaev. Optical Negative-Index Metamaterials. *Nat. Photon.*, **1**, 41, 2007.
- [12] Z. J. Wong, Y. Wang, K. O’Brien, J. Rho, X. Yin, S. Zhang, N. Fang, T.-J. Yen, and X. Zhang. Optical and Acoustic Metamaterials: Superlens, Negative Refractive Index and Invisibility Cloak. *J. Opt.*, **19**, 084007, 2017.
- [13] A. Poddubny, I. Iorsh, P. Belov, and Y. Kivshar. Hyperbolic Metamaterials. *Nat. Photon.*, **7**, 958–967, 2013.

- [14] Z. Wang, F. Cheng, T. Winsor, and Y. Liu. Optical Chiral Metamaterials: A Review of the Fundamentals, Fabrication Methods and Applications. *Nanotechnology*, **27**, 412001, 2016.
- [15] N. Ganesh, W. Zhang, P. C. Mathias, E. Chow, J. A. N. T. Soares, V. Mal-yarchuk, A. D. Smith, and B. T. Cunningham. Enhanced Fluorescence Emission from Quantum Dots on a Photonic Crystal Surface. *Nat. Nanotech.*, **2**, 515–520, 2007.
- [16] A. Shevchenko, V. Ovchinnikov, and A. Shevchenko. Large-Area Nanostructured Substrates for Surface Enhanced Raman Spectroscopy. *Appl. Phys. Lett.*, **100**, 171913, 2012.
- [17] R. Verre, M. Svedendahl, N. O. Länk, Z. J. Yang, G. Zengin, T. J. Antosiewicz, and M. Käll. Directional Light Extinction and Emission in a Metasurface of Tilted Plasmonic Nanopillars. *Nano Lett.*, **16**, 98–104, 2016.
- [18] Y. Sun and S. R. Forrest. Enhanced Light Out-Coupling of Organic Light-Emitting Devices Using Embedded Low-Index Grids. *Nat. Photon.*, **2**, 483, 2008.
- [19] J. J. Wierer, Jr, A. David, and M. M. Megens. III-Nitride Photonic-Crystal Light-Emitting Diodes with High Extraction Efficiency. *Nat. Photon.*, **3**, 163–169, 2009.
- [20] W. H. Koo, S. M. Jeong, F. Araoka, K. Ishikawa, S. Nishimura, T. Toyooka, and H. Takezoe. Light Extraction from Organic Light-Emitting Diodes Enhanced by Spontaneously Formed Buckles. *Nat. Photon.*, **4**, 222, 2010.
- [21] K. Nozaki, T. Tanabe, A. Shinya, S. Matsuo, T. Sato, H. Taniyama, and M. Notomi. Sub-Femtojoule All-Optical Switching Using a Photonic-Crystal Nanocavity. *Nat. Photon.*, **4**, 477–483, 2010.
- [22] M. R. Shcherbakov, P. P. Vabishchevich, A. S. Shorokhov, K. E. Chong, D.-Y. Choi, I. Staude, A. E. Miroshnichenko, D. N. Neshev, A. A. Fedyanin, and Y. S. Kivshar. Ultrafast All-Optical Switching with Magnetic Resonances in Nonlinear Dielectric Nanostructures. *Nano Lett.*, **15**, 6985–6990, 2015.
- [23] V.-C. Su, C. H. Chu, G. Sun, and D. P. Tsai. Advances in Optical Metasurfaces: Fabrication and Applications [Invited]. *Opt. Express*, **26**, 13148–13182, 2018.
- [24] T. Tanaka. Fabrication Techniques for Three-Dimensional Optical Metamaterials. In K. Sakoda, editor, *Electromagnetic Metamaterials: Modern Insights into Macroscopic Electromagnetic Fields*, Springer Series in Materials Science, 7–42. Springer, Singapore, 2019.
- [25] P. Minzioni, C. Lacava, T. Tanabe, J. Dong, X. Hu, G. Csaba, W. Porod, G. Singh, A. E. Willner, A. Almain, V. Torres-Company, J. Schröder, A. C. Peacock, M. J. Strain, F. Parmigiani, G. Contestabile, D. Marpaung, Z. Liu, J. E. Bowers, L. Chang, S. Fabbri, M. R. Vázquez, V. Bharadwaj, S. M. Eaton, P. Lodahl, X. Zhang, B. J. Eggleton, W. J. Munro, K. Nemoto, O. Morin, J. Laurat, and J. Nunn. Roadmap on All-Optical Processing. *J. Opt.*, **21**, 063001, 2019.
- [26] F. Mitsche. *Fiber Optics*. Springer, first edition, 2009.
- [27] Newport: High Speed Fiber-Optic Detectors. <https://www.newport.com/c/high-speed-fiber-optic-detectors>, 2020.
- [28] A. V. Krishnamoorthy, K. W. Goossen, W. Jan, X. Zheng, R. Ho, G. Li, R. Rozier, F. Liu, D. Patil, J. Lexau, H. Schwetman, D. Feng, M. Asghari, T. Pinguet, and J. E. Cunningham. Progress in Low-Power Switched Optical Interconnects. *IEEE J. Sel. Top. Quantum Electron.*, **17**, 357–376, 2011.

- [29] E. G. Sauter. *Nonlinear Optics*. Wiley, 1996.
- [30] M. Sheik-Bahae, J. Wang, and E. Van Stryland. Nondegenerate Optical Kerr Effect in Semiconductors. *IEEE J. Quantum Electron.*, **30**, 249–255, 1994.
- [31] S. Hooker and C. Webb. *Laser Physics*. Oxford University Press, 2010.
- [32] B. E. A. Saleh and M. C. Teich. *Fundamentals of Photonics*. Wiley, second edition, 2007.
- [33] J. Xie, X. Niu, X. Hu, F. Wang, Z. Chai, H. Yang, and Q. Gong. Ultracompact All-Optical Full-Adder and Half-Adder Based on Nonlinear Plasmonic Nanocavities. *Nanophotonics*, **6**, 1161–1173, 2017.
- [34] C. Koos, P. Vorreau, T. Vallaitis, P. Dumon, W. Bogaerts, R. Baets, B. Esem-
beson, I. Biaggio, T. Michinobu, F. Diederich, W. Freude, and J. Leuthold. All-Optical High-Speed Signal Processing with Silicon–Organic Hybrid Slot Waveguides. *Nat. Photon.*, **3**, 216–219, 2009.
- [35] M. Pu, H. Hu, L. Ottaviano, E. Semenova, D. Vukovic, L. K. Oxenløwe, and K. Yvind. Ultra-Efficient and Broadband Nonlinear AlGaAs-on-Insulator Chip for Low-Power Optical Signal Processing. *Laser & Photon. Rev.*, **12**, 1800111, 2018.
- [36] L. Ferrari, D. Lu, D. Lepage, and Z. Liu. Enhanced Spontaneous Emission inside Hyperbolic Metamaterials. *Opt. Express*, **22**, 4301, 2014.
- [37] T. Galfsky, H. N. S. Krishnamoorthy, W. Newman, E. E. Narimanov, Z. Jacob, and V. M. Menon. Active Hyperbolic Metamaterials: Enhanced Spontaneous Emission and Light Extraction. *Optica*, **2**, 62–65, 2015.
- [38] D. Lu, J. J. Kan, E. E. Fullerton, and Z. Liu. Enhancing Spontaneous Emission Rates of Molecules Using Nanopatterned Multilayer Hyperbolic Metamaterials. *Nat. Nanotechnol.*, **9**, 48–53, 2014.
- [39] A. Alù, M. G. Silveirinha, A. Salandrino, and N. Engheta. Epsilon-near-Zero Metamaterials and Electromagnetic Sources: Tailoring the Radiation Phase Pattern. *Phys. Rev. B*, **75**, 155410, 2007.
- [40] J. D. Jackson. *Classical Electrodynamics*. Wiley, second edition, 1975.
- [41] C. R. Simovski. Bloch Material Parameters of Magneto-Dielectric Metamaterials and the Concept of Bloch Lattices. *Metamaterials*, **1**, 62–80, 2007.
- [42] P. Grahm, A. Shevchenko, and M. Kaivola. Electromagnetic Multipole Theory for Optical Nanomaterials. *New J. Phys.*, **14**, 093033, 2012.
- [43] S. O’Brien and J. B. Pendry. Magnetic Activity at Infrared Frequencies in Structured Metallic Photonic Crystals. *J. Phys.: Condens. Matter*, **14**, 6383, 2002.
- [44] C. Menzel, C. Rockstuhl, T. Paul, F. Lederer, and T. Pertsch. Retrieving Effective Parameters for Metamaterials at Oblique Incidence. *Phys. Rev. B*, **77**, 195328, 2008.
- [45] M. G. Silveirinha. Metamaterial Homogenization Approach with Application to the Characterization of Microstructured Composites with Negative Parameters. *Phys. Rev. B*, **75**, 115104, 2007.
- [46] V. Kivijärvi, M. Nyman, A. Kärtilä, P. Grahm, A. Shevchenko, and M. Kaivola. Interaction of Metamaterials with Optical Beams. *New J. Phys.*, **17**, 063019, 2015.

- [47] L. Novotny and B. Hecht. *Principles of Nano-Optics*. Cambridge University Press, 2006.
- [48] P. W. Milonni. *The Quantum Vacuum: An Introduction to Quantum Electrodynamics*. Academic Press, 1994.
- [49] J. P. Reithmaier, G. Şek, A. Löffler, C. Hofmann, S. Kuhn, S. Reitzenstein, L. V. Keldysh, V. D. Kulakovskii, T. L. Reinecke, and A. Forchel. Strong Coupling in a Single Quantum Dot–Semiconductor Microcavity System. *Nature*, **432**, 197–200, 2004.
- [50] M. S. Skolnick, T. A. Fisher, and D. M. Whittaker. Strong Coupling Phenomena in Quantum Microcavity Structures. *Semicond. Sci. Technol.*, **13**, 645–669, 1998.
- [51] M. Kasperczyk, S. Person, D. Ananias, L. D. Carlos, and L. Novotny. Excitation of Magnetic Dipole Transitions at Optical Frequencies. *Phys. Rev. Lett.*, **114**, 163903, 2015.
- [52] P. Yao, C. Van Vlack, A. Reza, M. Patterson, M. M. Dignam, and S. Hughes. Ultrahigh Purcell Factors and Lamb Shifts in Slow-Light Metamaterial Waveguides. *Phys. Rev. B*, **80**, 195106, 2009.
- [53] S. R. J. Brueck. Radiation from a Dipole Embedded in a Dielectric Slab. *IEEE J. Sel. Topics Quantum Electron.*, **6**, 899, 2000.
- [54] K. Sainath, F. L. Teixeira, and B. Donderici. Robust Computation of Dipole Electromagnetic Fields in Arbitrarily Anisotropic, Planar-Stratified Environments. *Phys. Rev. E*, **89**, 013312, 2014.
- [55] L. Pazynin, S. Sautbekov, Y. Sirenko, A. Vertiy, and N. Yashina. Green’s Function for an Infinite Anisotropic Medium. Review. *Telecom. Rad. Eng.*, **74**, 1039, 2015.
- [56] J. A. Kong. Electromagnetic Fields Due to Dipole Antennas over Stratified Anisotropic Media. *Geophys.*, **37**, 985, 1972.
- [57] X. Ni, G. V. Naik, A. V. Kildishev, Y. Barnakov, A. Boltasseva, and V. M. Shalaev. Effect of Metallic and Hyperbolic Metamaterial Surfaces on Electric and Magnetic Dipole Emission Transitions. *Appl. Phys. B*, **103**, 553–558, 2011.
- [58] R. C. McPhedran, L. C. Botten, J. McOrist, A. A. Asatryan, C. M. de Sterke, and N. A. Nicorovici. Density of States Functions for Photonic Crystals. *Phys. Rev. E*, **69**, 016609, 2004.
- [59] K. Ujihara, A. Nakamura, O. Manba, and X.-P. Feng. Spontaneous Emission in a Very Short Optical Cavity with Plane-Parallel Dielectric Mirrors. *Jpn. J. Appl. Phys.*, **30**, 3388, 1991.
- [60] G. P. Ortiz and W. L. Mochán. Nonadditivity of Poynting Vector within Opaque Media. *J. Opt. Soc. Am. A*, **22**, 2827–2837, 2005.
- [61] V. Kivijärvi, M. Nyman, A. Shevchenko, and M. Kaivola. Optical-Image Transfer through a Diffraction-Compensating Metamaterial. *Opt. Express*, **24**, 9806–9815, 2016.
- [62] V. Kivijärvi, M. Nyman, A. Shevchenko, and M. Kaivola. An Optical Metamaterial with Simultaneously Suppressed Optical Diffraction and Surface Reflection. *J. Opt.*, **18**, 035103, 2016.
- [63] V. Kivijärvi, M. Nyman, A. Shevchenko, and M. Kaivola. Theoretical Description and Design of Nanomaterial Slab Waveguides: Application to Compensation of Optical Diffraction. *Opt. Express*, **26**, 9134–9147, 2018.

- [64] D. J. Griffiths. *Introduction to Electrodynamics*. Prentice Hall, third edition, 1999.
- [65] M. G. Silveirinha. Poynting Vector, Heating Rate, and Stored Energy in Structured Materials: A First-Principles Derivation. *Phys. Rev. B*, **80**, 235120, 2009.
- [66] A. M. Kern, D. Zhang, M. Brecht, A. I. Chizhik, A. V. Failla, F. Wackenhut, and A. J. Meixner. Enhanced Single-Molecule Spectroscopy in Highly Confined Optical Fields: From $\lambda/2$ -Fabry–Pérot Resonators to Plasmonic Nano-Antennas. *Chem. Soc. Rev.*, **43**, 1263–1286, 2014.
- [67] M. D. Barnes, W. B. Whitten, S. Arnold, and J. M. Ramsey. Homogeneous Linewidths of Rhodamine 6G at Room Temperature from Cavity-enhanced Spontaneous Emission Rates. *J. Chem. Phys.*, **97**, 7842–7845, 1992.
- [68] G. Shambat, B. Ellis, A. Majumdar, J. Petykiewicz, M. A. Mayer, T. Sarmiento, J. Harris, E. E. Haller, and J. Vučković. Ultrafast Direct Modulation of a Single-Mode Photonic Crystal Nanocavity Light-Emitting Diode. *Nat. Comm.*, **2**, 539, 2011.
- [69] S. Gupta and E. Waks. Overcoming Auger Recombination in Nanocrystal Quantum Dot Laser Using Spontaneous Emission Enhancement. *Opt. Express*, **22**, 3013–3027, 2014.
- [70] S. Li, J. He, and Q.-H. Xu. Aggregation of Metal-Nanoparticle-Induced Fluorescence Enhancement and Its Application in Sensing. *ACS Omega*, **5**, 41–48, 2019.
- [71] R. J. Potton. Reciprocity in Optics. *Rep. Prog. Phys.*, **67**, 717, 2004.
- [72] M. Araki, H. Koyama, and N. Koshida. Precisely Tuned Emission from Porous Silicon Vertical Optical Cavity in the Visible Region. *J. Appl. Phys.*, **80**, 4841–4844, 1996.
- [73] A. Coens, M. Chakaroun, A. P. A. Fischer, M. W. Lee, A. Boudrioua, B. Gefroy, and G. Vemuri. Experimental Optimization of the Optical and Electrical Properties of a Half-Wavelength-Thick Organic Hetero-Structure in a Micro-Cavity. *Opt. Express*, **20**, 29252–29259, 2012.
- [74] D. G. Deppe and C. Lei. Spontaneous Emission and Optical Gain in a Fabry–Perot Microcavity. *Appl. Phys. Lett.*, **60**, 527–529, 1992.
- [75] G. J. Lee, B. Y. Jung, C. K. Hwangbo, and J. S. Yoon. Photoluminescence Characteristics in Metal-Distributed Feedback-Mirror Microcavity Containing Luminescent Polymer and Filler. *Jpn. J. Appl. Phys.*, **41**, 5241, 2002.
- [76] C. Lei, Z. Huang, D. G. Deppe, C. J. Pinzone, and R. D. Dupuis. Spectral Interference Effects in the Light Emission from Fabry-Perot Cavities. *J. Appl. Phys.*, **73**, 2700–2704, 1992.
- [77] C. B. Walsh and E. I. Franses. Ultrathin PMMA Films Spin-Coated from Toluene Solutions. *Thin Solid Films*, **429**, 71–76, 2003.
- [78] M. Decker, I. Staude, I. I. Shishkin, K. B. Samusev, P. Parkinson, V. K. A. Sreenivasan, A. Minovich, A. E. Miroshnichenko, A. Zvyagin, C. Jagadish, D. N. Neshev, and Y. S. Kivshar. Dual-Channel Spontaneous Emission of Quantum Dots in Magnetic Metamaterials. *Nat. Comm.*, **4**, 2949, 2013.

- [79] P. K. Badiya, S. G. Patnaik, V. Srinivasan, N. Reddy, C. S. Manohar, R. Vedarajan, N. Mastumi, S. K. Belliraj, and S. S. Ramamurthy. Ag-Protein Plasmonic Architectures for Surface Plasmon-Coupled Emission Enhancements and Fabry-Perot Mode-Coupled Directional Fluorescence Emission. *Chem. Phys. Lett.*, **685**, 139–145, 2017.
- [80] S. Joosten, E. Kaczanowicz, M. Ungaro, M. Reh fuss, K. Johnston, and Z. E. Meziani. Enhanced UV Light Detection Using a P-Terphenyl Wavelength Shifter. *Nuclear Instruments and Methods in Physics Research Section A: Accelerators, Spectrometers, Detectors and Associated Equipment*, **870**, 110–115, 2017.
- [81] S. Wu, B. Liu, Z. Zhu, C. Cheng, H. Chen, M. Gu, L. Chen, J. Liu, X. Ouyang, C. Xue, and Y. Wu. Guided-Mode Resonance Assisted Directional Emission of a Wavelength-Shifting Film for Application in Scintillation Detection. *Opt. Express*, **24**, 231–238, 2016.
- [82] T. Yagi, T. Misawa, C. H. Pyeon, and S. Shiroya. A Small High Sensitivity Neutron Detector Using a Wavelength Shifting Fiber. *Appl. Radiat. Isotop.*, **69**, 176–179, 2011.
- [83] G. Ghosh. Dispersion-Equation Coefficients for the Refractive Index and Birefringence of Calcite and Quartz Crystals. *Optics Communications*, **163**, 95–102, 1999.
- [84] RefractiveIndex.Info. <https://refractiveindex.info>, 2020.
- [85] K. B. Rochford, A. H. Rose, P. A. Williams, C. M. Wang, I. G. Clarke, P. D. Hale, and G. W. Day. Design and Performance of a Stable Linear Retarder. *Appl. Opt.*, **36**, 6458–6465, 1997.
- [86] J. M. Herrera-Fernandez, J. L. Vilas, L. M. Sanchez-Brea, and E. Bernabeu. Design of Superachromatic Quarter-Wave Retarders in a Broad Spectral Range. *Appl. Opt.*, **54**, 9758–9762, 2015.
- [87] A. Messaadi, M. M. Sánchez-López, A. Vargas, P. García-Martínez, and I. Moreno. Achromatic Linear Retarder with Tunable Retardance. *Opt. Lett.*, **43**, 3277–3280, 2018.
- [88] T. Peters, S. S. Ivanov, D. Englisch, A. A. Rangelov, N. V. Vitanov, and T. Halfmann. Variable Ultrabroadband and Narrowband Composite Polarization Retarders. *Appl. Opt.*, **51**, 7466–7474, 2012.
- [89] B. Päivänranta, N. Passilly, J. Pietarinen, P. Laakkonen, M. Kuittinen, and J. Tervo. Low-Cost Fabrication of Form-Birefringent Quarter-Wave Plates. *Opt. Express*, **16**, 16334, 2008.
- [90] J. P. Balthasar Mueller, N. A. Rubin, R. C. Devlin, B. Groever, and F. Capasso. Metasurface Polarization Optics: Independent Phase Control of Arbitrary Orthogonal States of Polarization. *Phys. Rev. Lett.*, **118**, 113901, 2017.
- [91] A. Arbabi, Y. Horie, M. Bagheri, and A. Faraon. Dielectric Metasurfaces for Complete Control of Phase and Polarization with Subwavelength Spatial Resolution and High Transmission. *Nat. Nanotechnol.*, **10**, 937–943, 2015.
- [92] A. Kravchenko, A. Shevchenko, V. Ovchinnikov, P. Grahn, and M. Kaivola. Fabrication and Characterization of a Large-Area Metal Nano-Grid Wave Plate. *Appl. Phys. Lett.*, **103**, 033111, 2013.
- [93] A. Roberts and L. Lin. Plasmonic Quarter-Wave Plate. *Opt. Lett.*, **37**, 1820–1822, 2012.

- [94] Y. Zhao and A. Alù. Manipulating Light Polarization with Ultrathin Plasmonic Metasurfaces. *Phys. Rev. B*, **84**, 205428, 2011.
- [95] F. Ding, Z. Wang, S. He, V. M. Shalaev, and A. V. Kildishev. Broadband High-Efficiency Half-Wave Plate: A Supercell-Based Plasmonic Metasurface Approach. *ACS Nano*, **9**, 4111–4119, 2015.
- [96] N. Yu, F. Aieta, P. Genevet, M. A. Kats, Z. Gaburro, and F. Capasso. A Broadband, Background-Free Quarter-Wave Plate Based on Plasmonic Metasurfaces. *Nano Lett.*, **12**, 6328–6333, 2012.
- [97] S. Maurya, M. Nyman, M. Kaivola, and A. Shevchenko. Highly Birefringent Metamaterial Structure as a Tunable Partial Polarizer. *Opt. Express*, **27**, 27335–27344, 2019.
- [98] Y. J. Shin, C. Pina-Hernandez, Y.-K. Wu, J. G. Ok, and L. J. Guo. Facile Route of Flexible Wire Grid Polarizer Fabrication by Angled-Evaporations of Aluminum on Two Sidewalls of an Imprinted Nanograting. *Nanotechnology*, **23**, 344018, 2012.
- [99] D. Xia, Z. Ku, S. C. Lee, and S. R. J. Brueck. Nanostructures and Functional Materials Fabricated by Interferometric Lithography. *Adv. Mat.*, **23**, 147–179, 2011.
- [100] H. Schift. Nanoimprint Lithography: An Old Story in Modern Times? A Review. *J. Vac. Sci. Technol. B*, **26**, 458–480, 2008.
- [101] K. Ikeda and Y. Fainman. Material and Structural Criteria for Ultra-Fast Kerr Nonlinear Switching in Optical Resonant Cavities. *Solid State Electron.*, **51**, 1376–1380, 2007.
- [102] K. Narayanan and S. F. Preble. Optical Nonlinearities in Hydrogenated-Amorphous Silicon Waveguides. *Opt. Express*, **18**, 8998–9005, 2010.
- [103] A. M. Ionescu and H. Riel. Tunnel Field-Effect Transistors as Energy-Efficient Electronic Switches. *Nature*, **479**, 329–337, 2011.
- [104] B. T. Diroll, K. S. Schramke, P. Guo, U. R. Kortshagen, and R. D. Schaller. Ultrafast Silicon Photonics with Visible to Mid-Infrared Pumping of Silicon Nanocrystals. *Nano Lett.*, **17**, 6409–6414, 2017.
- [105] W. W. Chow, S. W. Koch, and M. Sargent III. *Semiconductor-Laser Physics*. Springer-Verlag, 1994.
- [106] L. A. Coldren and S. W. Corzine. *Diode Lasers and Photonic Integrated Circuits*. Wiley, 1995.
- [107] K. Tajima. All-Optical Switch with Switch-Off Time Unrestricted by Carrier Lifetime. *Jpn. J. Appl. Phys.*, **32**, L1746, 1993.
- [108] X. Yang and W. Hu. Principle and Applications of Semiconductor Optical Amplifiers-Based Turbo-Switches. *Front. Optoelectron.*, **9**, 346–352, 2016.
- [109] I. Rendón-Salgado, E. Ramírez-Cruz, and R. Gutiérrez-Castrejón. 640 Gb/s All-Optical AND Gate and Wavelength Converter Using Bulk SOA Turbo-Switched Mach-Zehnder Interferometer with Improved Differential Scheme. *Opt. & Laser Technol.*, **109**, 671–681, 2019.
- [110] M. Wefers and K. Nelson. Space-Time Profiles of Shaped Ultrafast Optical Waveforms. *IEEE J. Quantum Electron.*, **32**, 161–172, 1996.
- [111] A. M. Weiner. Femtosecond Pulse Shaping Using Spatial Light Modulators. *Rev. Sci. Instrum.*, **71**, 1929–1960, 2000.

- [112] C. Ruckebusch, M. Sliwa, P. Pernot, A. de Juan, and R. Tauler. Comprehensive Data Analysis of Femtosecond Transient Absorption Spectra: A Review. *J. Photochem. Photobiol. C: Photochem. Rev.*, **13**, 1–27, 2012.
- [113] J. Liang and L. V. Wang. Single-Shot Ultrafast Optical Imaging. *Optica*, **5**, 1113–1127, 2018.
- [114] L. Gao, J. Liang, C. Li, and L. V. Wang. Single-Shot Compressed Ultrafast Photography at One Hundred Billion Frames per Second. *Nature*, **516**, 74–77, 2014.
- [115] J. T. Fourkas, L. Dhar, K. A. Nelson, and R. Trebino. Spatially Encoded, Single-Shot Ultrafast Spectroscopies. *J. Opt. Soc. Am. B*, **12**, 155–165, 1995.
- [116] Y. Makishima, N. Furukawa, A. Ishida, and J. Takeda. Femtosecond Real-Time Pump-Probe Imaging Spectroscopy Implemented on a Single Shot Basis. *Jpn. J. Appl. Phys.*, **45**, 5986, 2006.
- [117] M. Fujimoto, S. Aoshima, M. Hosoda, and Y. Tsuchiya. Femtosecond Time-Resolved Optical Polarigraphy: Imaging of the Propagation Dynamics of Intense Light in a Medium. *Opt. Lett.*, **24**, 850–852, 1999.
- [118] H.-Y. Huang, Z.-J. Cheng, Y. Yang, Q.-Y. Yue, and C.-S. Guo. Single-Shot Ultrafast Sequential Holographic Imaging with High Temporal Resolution and a Large Field of View. *Opt. Lett.*, **44**, 4885–4888, 2019.
- [119] K. Nakagawa, A. Iwasaki, Y. Oishi, R. Horisaki, A. Tsukamoto, A. Nakamura, K. Hirosawa, H. Liao, T. Ushida, K. Goda, F. Kannari, and I. Sakuma. Sequentially Timed All-Optical Mapping Photography (STAMP). *Nat. Photon.*, **8**, 695–700, 2014.
- [120] T. Suzuki, F. Isa, L. Fujii, K. Hirosawa, K. Nakagawa, K. Goda, I. Sakuma, and F. Kannari. Sequentially Timed All-Optical Mapping Photography (STAMP) Utilizing Spectral Filtering. *Opt. Express*, **23**, 30512–30522, 2015.
- [121] M. A. Foster, R. Salem, D. F. Geraghty, A. C. Turner-Foster, M. Lipson, and A. L. Gaeta. Silicon-Chip-Based Ultrafast Optical Oscilloscope. *Nature*, **456**, 81–84, 2008.
- [122] A. Krishnan, L. G. de Peralta, V. Kuryatkov, A. A. Bernussi, and H. Temkin. Direct Space-to-Time Pulse Shaper with Reflective Arrayed Waveguide Gratings and Phase Masks. *Opt. Lett.*, **31**, 640–642, 2006.
- [123] A. Vega, D. E. Leaird, and A. M. Weiner. High-Speed Direct Space-to-Time Pulse Shaping with 1 Ns Reconfiguration. *Opt. Lett.*, **35**, 1554–1556, 2010.



ISBN 978-952-64-0288-8 (printed)
ISBN 978-952-64-0289-5 (pdf)
ISSN 1799-4934 (printed)
ISSN 1799-4942 (pdf)

Aalto University
School of Science
Department of Applied Physics
www.aalto.fi

**BUSINESS +
ECONOMY**

**ART +
DESIGN +
ARCHITECTURE**

**SCIENCE +
TECHNOLOGY**

CROSSOVER

**DOCTORAL
DISSERTATIONS**